Microalloying induced stable welded interfaces for highly reversible zero-excess sodium metal batteries

Chunlin Xie, [a] Hao Wu, [a] Kang Liang, [b] Zhengping Ding, [b] Jiawen Dai, [a] Rui Zhang, [a] Yurong Ren, [b] Yixin Li, [a] Dan Sun, [a] Qi Zhang, [a] Yougen Tang, [a] Haiyan Wang [a]*

 [a]Hunan Provincial Key Laboratory of Chemical Power Sources

College of Chemistry and Chemical Engineering

Central South University

Changsha, 410083, P.R. China

[b]Jiangsu Province Engineering Research Center of Intelligent Manufacturing Technology for the New Energy Vehicle Power Battery

School of Materials Science and Engineering

Changzhou University

Changzhou, 213164 P. R. China

E-mail: wanghy419@csu.edu.cn

Methods

Material preparation.

Metal tin and zinc targets with a diameter of 10 cm (99.99% purity) were purchased from ONA Targets Ltd. Magnetron sputtering equipment manufactured by TAILONG ElECTRONICS (Sputter-100). The Al@C foil serving as a substrate for sputtering, the chamber was evacuated to a pressure lower than 5.0×10^{-6} Pa before sputtering, and the Ar gases were injected into the chamber at a flow rate of 100 sccm. The Al@C-Zn was acquired through a 5 min sputtering process of a pure antimony target utilizing a 200 W RF power supply. In order to obtain coatings with a similar thickness and particle size to Al@C-Zn, we set the preparation parameters for Al@C-Sn as follows: a power setting of 100 W for 3 min.

The sodium discs of 14 mm diameter, glass fibre (Whatman GF/A), Celgard C200 membrane and Al@C foil with a thickness of 14 μm were purchased from Canrd Technology Co. Ltd. The electrolyte was obtained by dissolving 0.9 M $NaPF_6$ (DoDoChem, battery grade) and 0.1 M $NaBF_4$ (ALADDIN, 99.9% metals basis) in diglyme (DoDoChem, battery grade). Carbon-coated $Na_3V_2(PO_4)_3$ cathode (NVP) was purchased from Shenzhen Kejing Ltd. The composition of the cathode slurry was 90wt% active materials, 5wt% Super P and 5wt% PVDF. The electrode slurries were cast on Al@C foil followed by a drying process under a vacuum. The mass loading of active cathode materials is ~10.4 mg cm^{-2}.

Characterizations.

In-situ X-ray diffraction (XRD) and grazing incidence XRD (GI-XRD) were recorded using a Bruker D8 X-ray diffractometer with monochromatized Cu Kα radiation (wavelength = 1.5406 Å). Nondestructive-XRD spectra enabling avoidance of air

contact were recorded using a Rigaku X-ray diffractometer. The scanning electron microscope (SEM, JSM-7610FPlus) with non-destructive transfer capability was used to characterize the sodium plating and stripping morphology of the substrate. The cross-section sample were subjected to focused ion beam (FIB, TESCAN AMBER) processing. The surface chemical composition was determined by X-ray photoelectron spectroscopy (XPS) using a PHI 5000 VersaProbe III instrument with an Al Kα X-ray source (Avoid exposure to air). Optical microscopy (AOSVI M203-HD228S) equipped with an in-situ reaction device was used to observe the evolution of sodium deposition. Transmission electron microscopy (TEM, JEOL/JEM-F200) was used to characterize the crystal structure of the nano-coated layers before and after the alloying reaction. Molybdenum mesh microgrids were coated with Nano-Zn (or Sn) layers using the magnetron sputtering method. The parameters of magnetron sputtering were adjusted to match the process parameters for the preparation of Al@C-Zn and Al@C-Sn, but the sputtering time was reduced by half to meet the sample thickness requirements during TEM testing. To investigate the structural changes of the coating after sodium plating/stripping, we assembled half-cells for repeated sodium plating/stripping using sputter-coated molybdenum mesh as electrodes. Afterward, a simple solvent cleaning was conducted to coated microgrids before direct utilization for TEM observations. The spatial distribution of SEI composition at the substrate interface was obtained using time-of-flight secondary ion mass spectrometry combined with ion beam etching (TOF-SIMS, With non-destructive transfer device, Thermo scientific Scios 2 Hivac, TOFWERK, 30 keV Ga ion sputter gun). The morphology of the nano-coated layer was characterized by using atomic force microscopy (AFM, Burker MultiMode). In this work, non-destructive transfer devices were used for XPS, SEM, XRD and TOF-SIMS tests, which adequately preserved the true information of the test samples (the samples

were handled in a glove box). The corresponding non-destructive transmission device

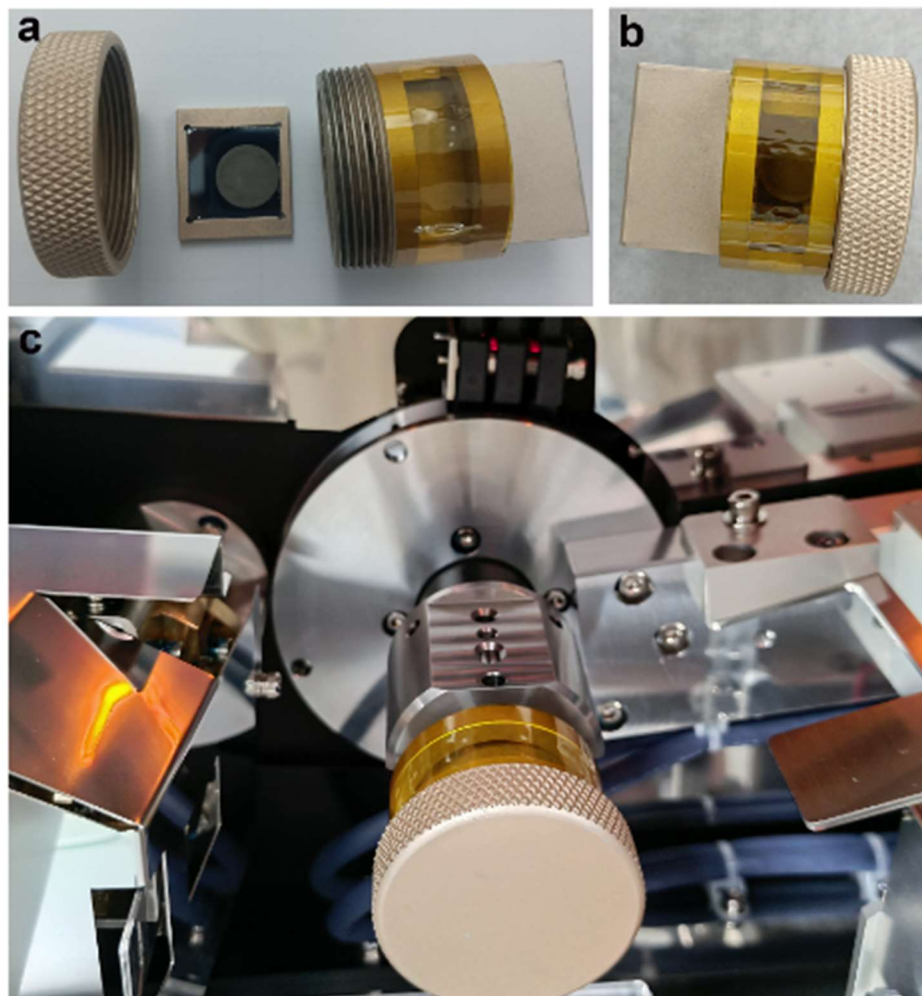and the process used are shown below (Figure D1-4):

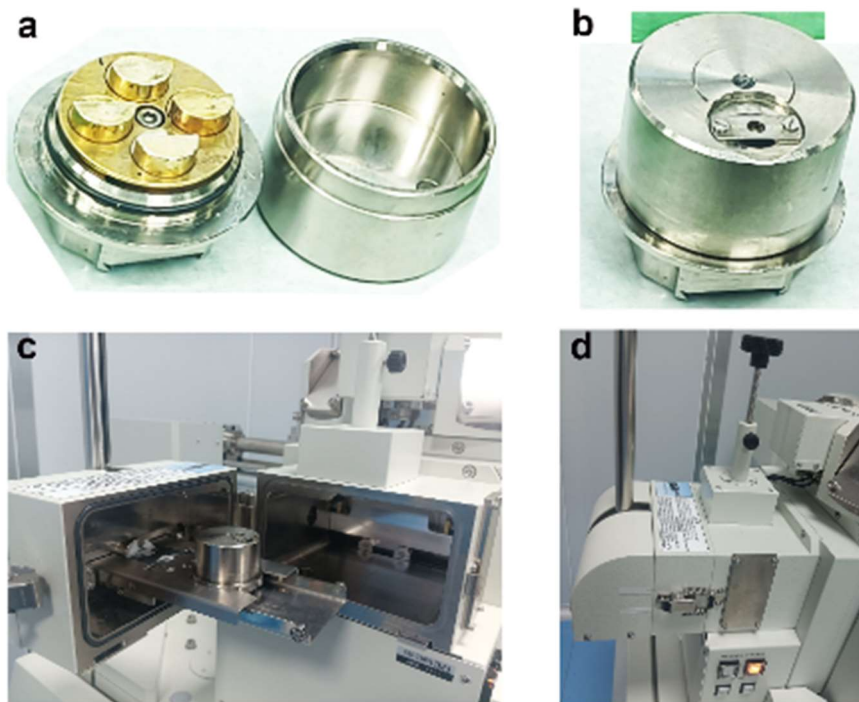**Figure D1.** Non-destructive transfer devices for XRD.

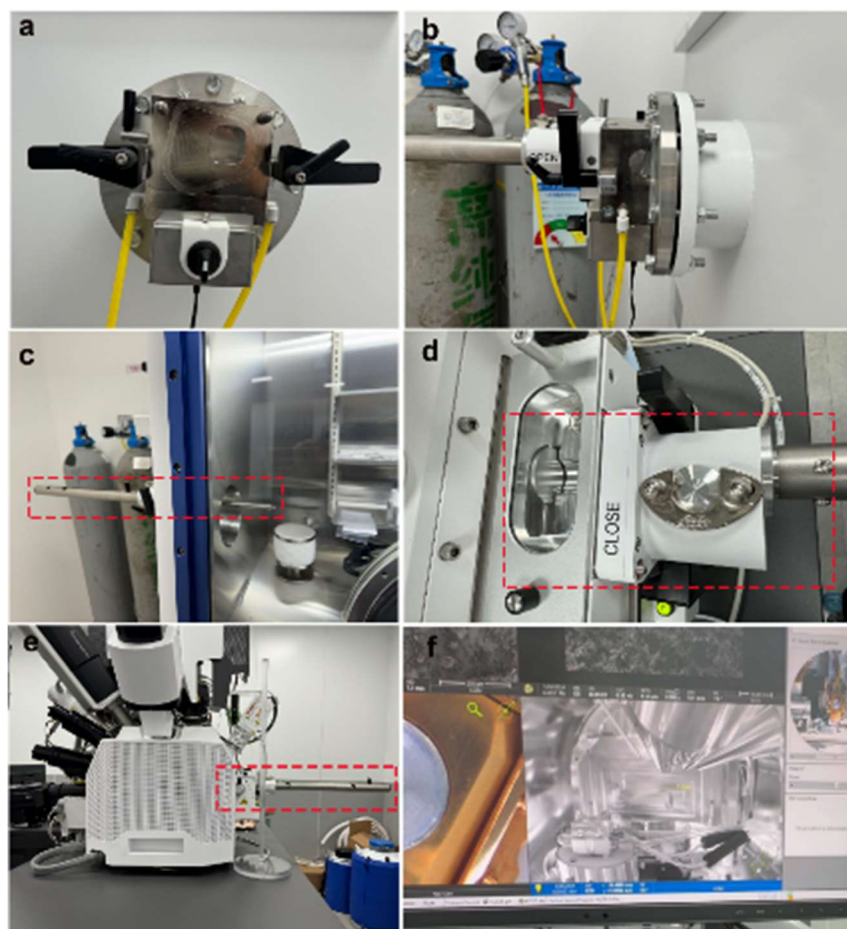**Figure D2.** Non-destructive transfer devices for SEM.

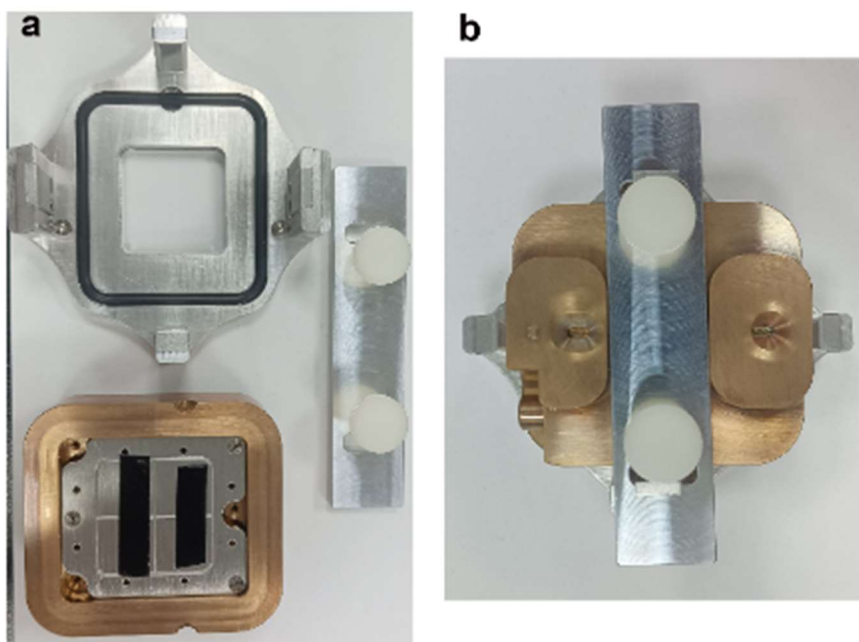**Figure D3.** Non-destructive transfer devices for TOF-SIMS.

Figure D4. Non-destructive transfer devices for XPS.

Electrochemical measurements.

Coin cells (CR2032) were assembled in an argon-filled glove box. The amount of electrolyte used for a coin cell is 100 μL. Glass fibre (Whatman GF/A) plus Celgard C200 membrane was utilized as the separator. The galvanostatic charge/discharge tests were performed using a Neware MIHW-200-160CH battery testing system. The zero-excess sodium metal battery did not perform any pre-treatment such as pre-sodiumation before cycling. The ZSMBs were activated five times using a current density of 50 mA g^{-1} before cycling with a current density of 300 mA g^{-1}. The charge cut-off voltage of the Na||Al@C (or Al@C-Zn and Al@C-Sn) half-cell was set to 0.5 V (vs Na/Na$^+$). The EIS was performed on the AUTOLAB electrochemical workstation with a frequency range of 0.01 Hz ~100 kHz. The EIS of full cells was tested at full charge state (charged to 3.8V). The cyclic voltammetry (CV) for half-cells (or full cells) was conducted on a CHI660E electrochemical workstation at a scanning rate of 1 mV s^{-1} with a voltage range of −0.05 ~ 1 V (2 ~ 3.8 V).

Computational details.

The first-principles calculations were conducted using generalized gradient approximation (GGA) and Perdew–Burke–Ernzerhof (PBE) exchange-correlation functional in Castep module of Materials Studio of Accelrys Inc. During geometry optimization, the convergence tolerance was set to 1.0×10^{-5} eV per atom for energy, 3.0×10^{-2} eV Å^{-1} for maximum force, and 1.0×10^{-3} Å for maximum displacement. The binding energy (E_b) is calculated according to the following equation:

$$E_b = E_{total} - E_{sub} - E_{atom} \qquad (1)$$

E_{total}, E_{sub}, and E_{atom} represent the total energy of the zinc facets (or Sn, C and Al facets) combined with the sodium atom, the energy of zinc facets (or Sn, C and Al facets), and the energy of the sodium atom, respectively.
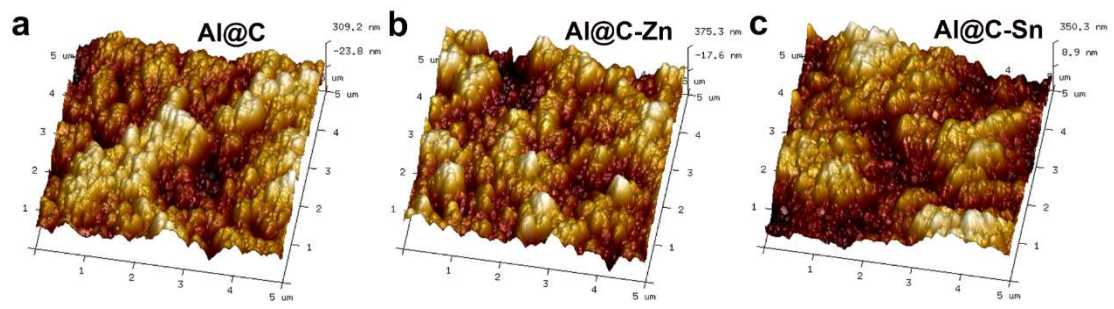
Figure S1. AFM images of Al@C foil，Al@C-Zn and Al@C-Sn surfaces
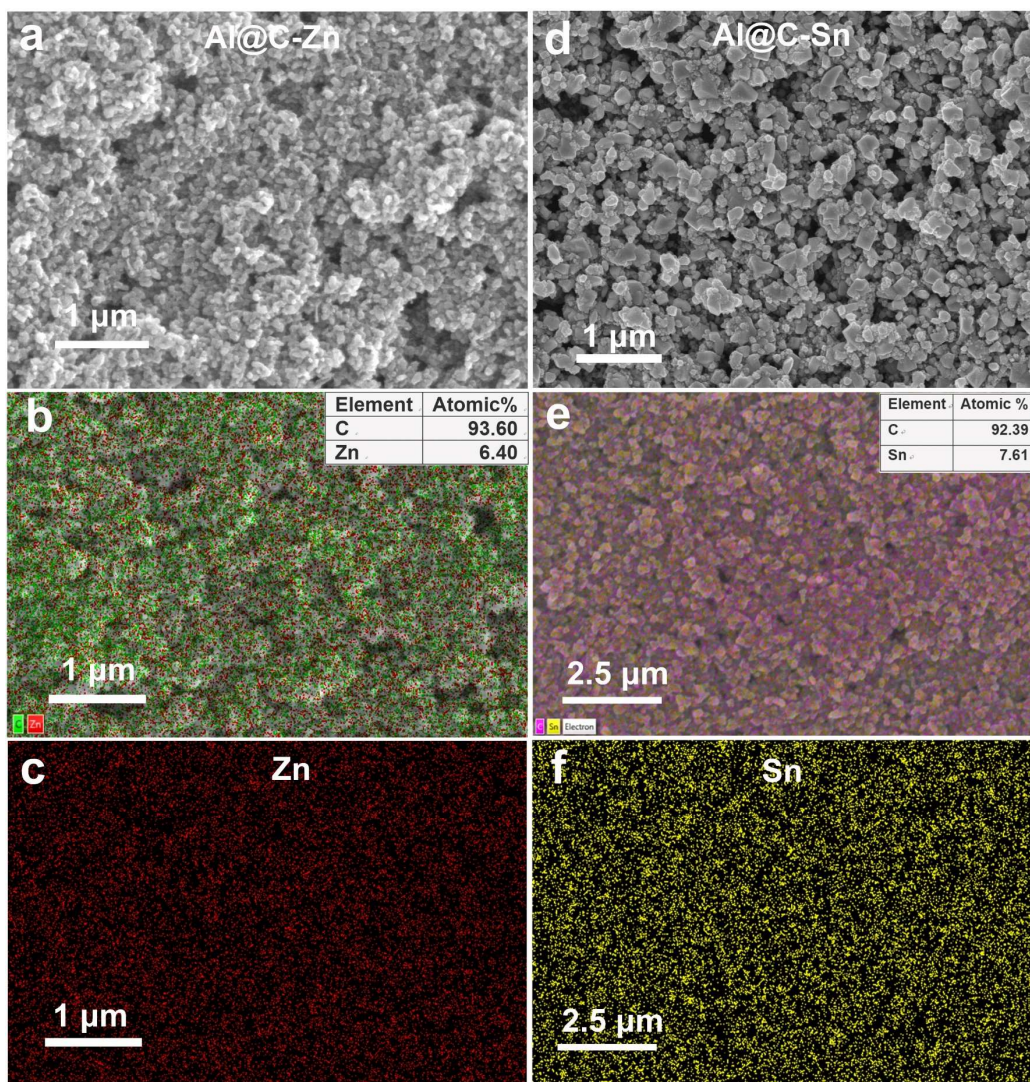
Figure S2. SEM images and EDS mappings of (a-c) Al@C-Zn and (d-f) Al@C-Sn.
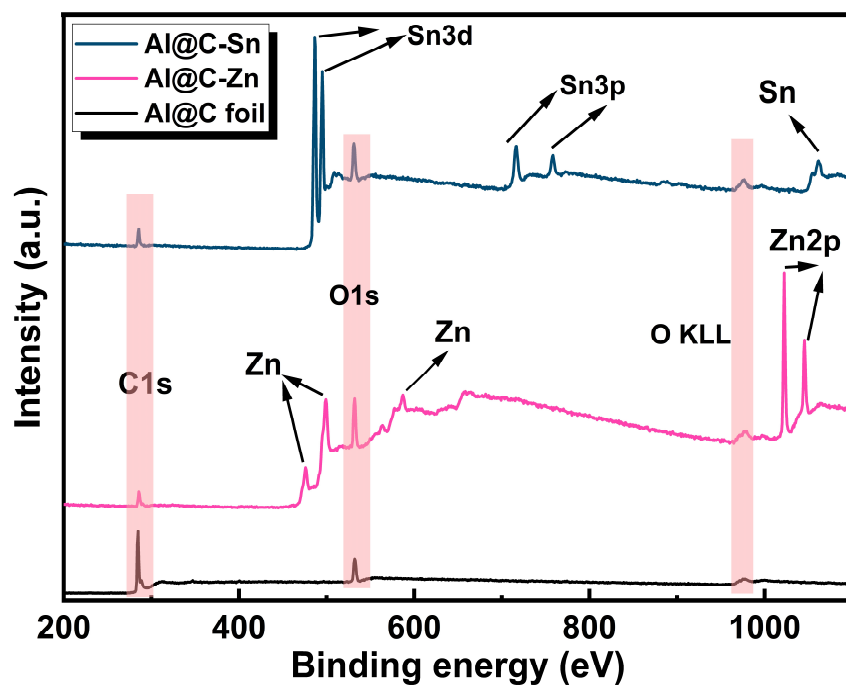
Figure S3. The XPS spectrum of Al@C foil, Al@C-Zn and Al@C-Sn.
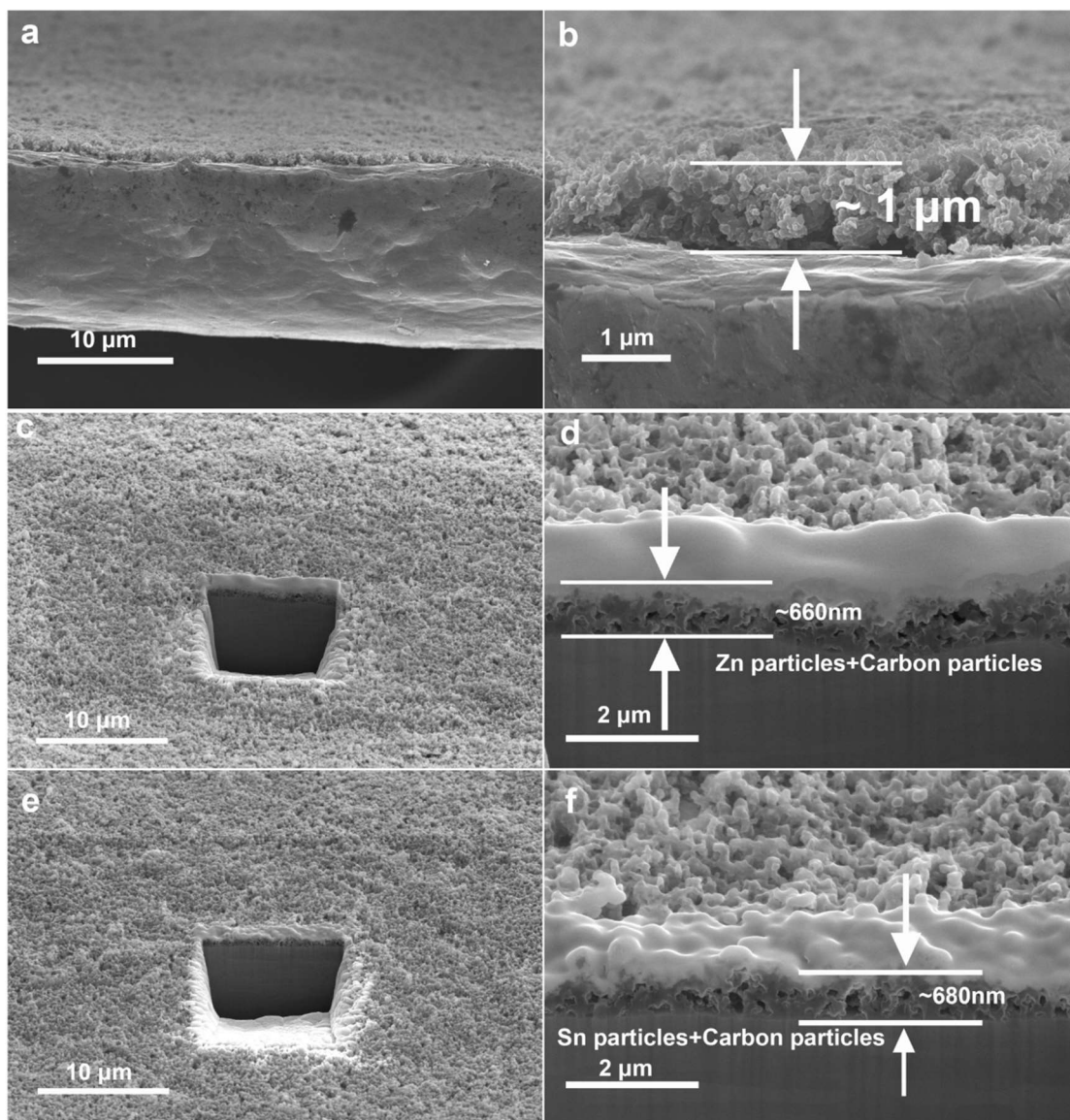
Figure S4. Cross-section SEM images of (a, b) Al@C foil, (c, d) Al@C-Zn and (e, f) Al@C-Sn processed by FIB.

It should be noted that the thickness of the carbon layer is significantly reduced due to the fact that the nanoparticles generated by magnetron sputtering will attack the carbon layer. Due to the limited resolution of the energy spectrum, the actual thickness of the magnetron sputtered coatings could not be measured accurately, and only the total thickness of the coatings and the carbon layer could be obtained. However, it can still be shown that the metal coating thicknesses of Al@C-Zn and Al@C-Sn are less than 660 nm and 680 nm, respectively.
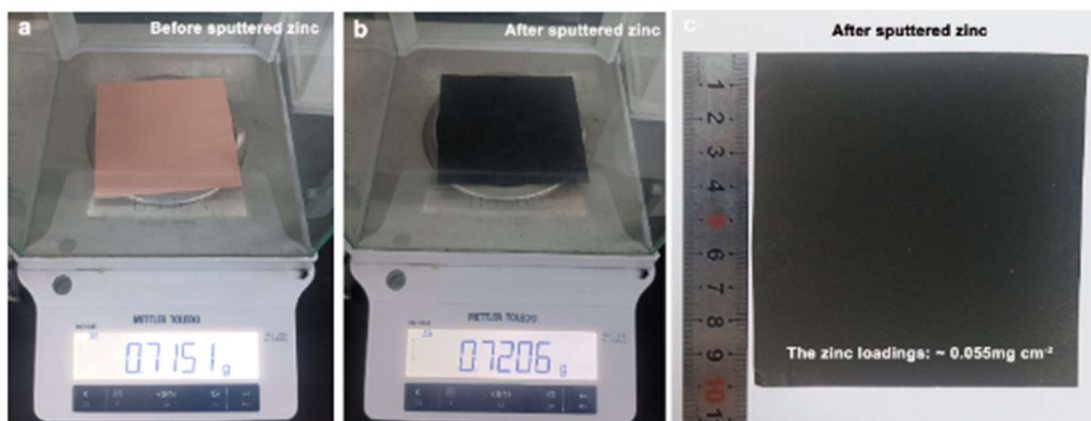
Figure S5. Mass of zinc layer on copper foil sputtered at 200 W for 5 min.

The sputtered zinc will bombard the carbon layer (the quality of the carbon layer will be affected), and thus the quality of the zinc layer cannot be precisely determined. To avoid this situation, a rough copper foil was used instead of Al@C foil to indirectly derive the mass of the zinc layer for the same sputtering parameters, which is about 0.055 mg cm^{-2} as shown in Figure S5. This mass does not significantly affect the energy density of the battery.
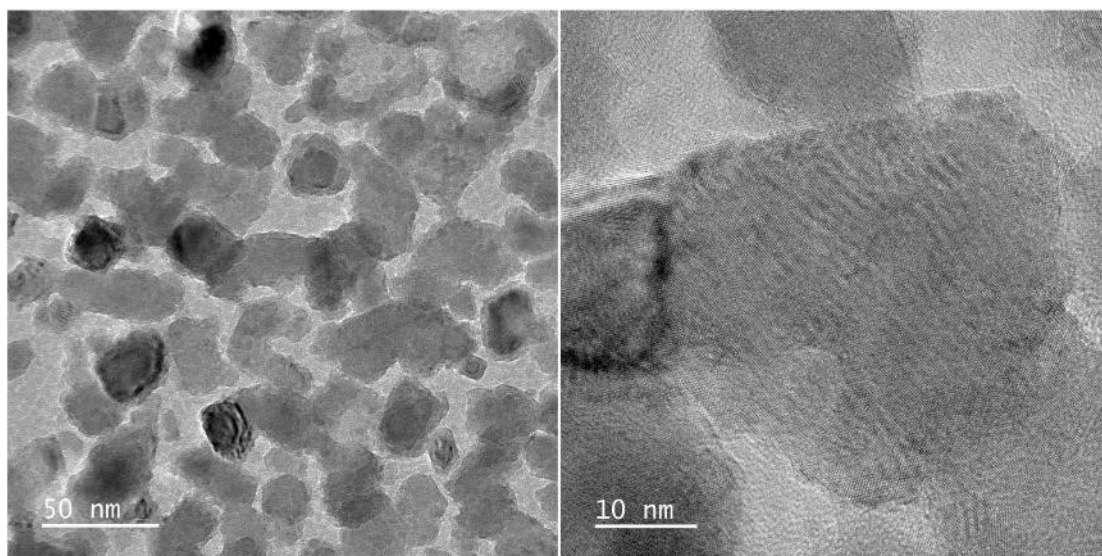
Figure S6. The TEM images of zinc particles sputtered on a molybdenum mesh microgrid.
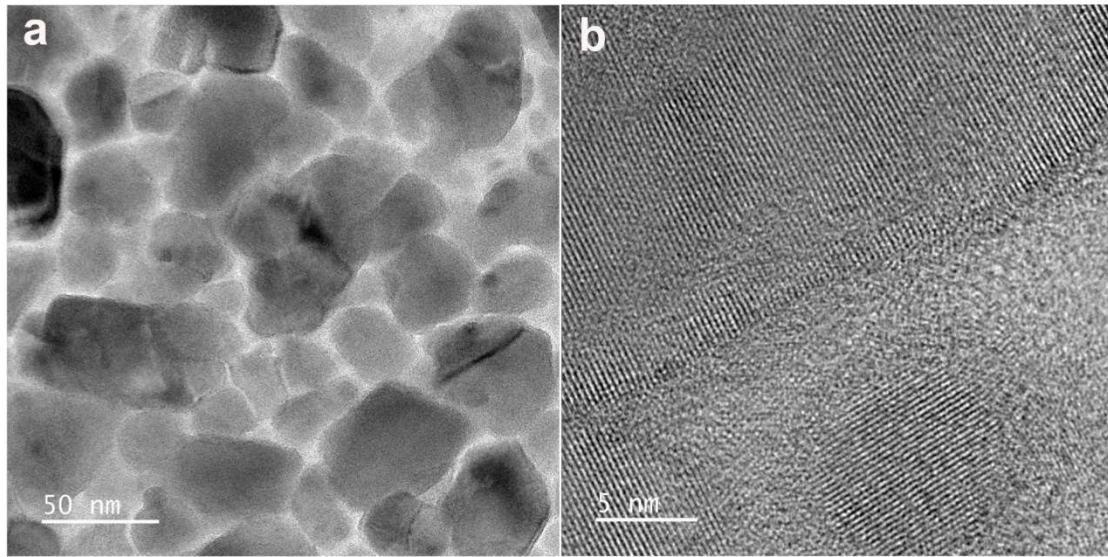
Figure S7. The TEM images of tin particles sputtered on a molybdenum mesh microgrid.
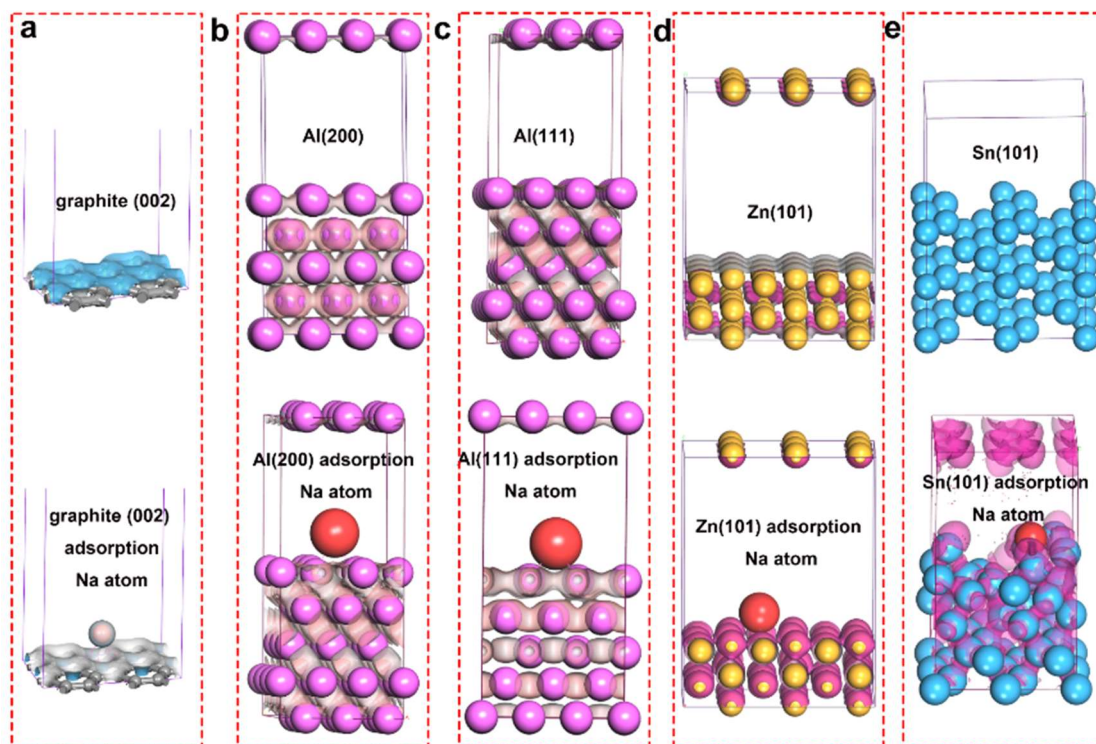
Figure S8. Lattice states of the (a) graphite (0 0 2) facet, (b) Al (2 0 0) facet, (c) Al(1 1 1) facet, (d) Zn(1 0 1) facet and (e) Sn (1 0 1) facet before and after adsorption of Na atom.
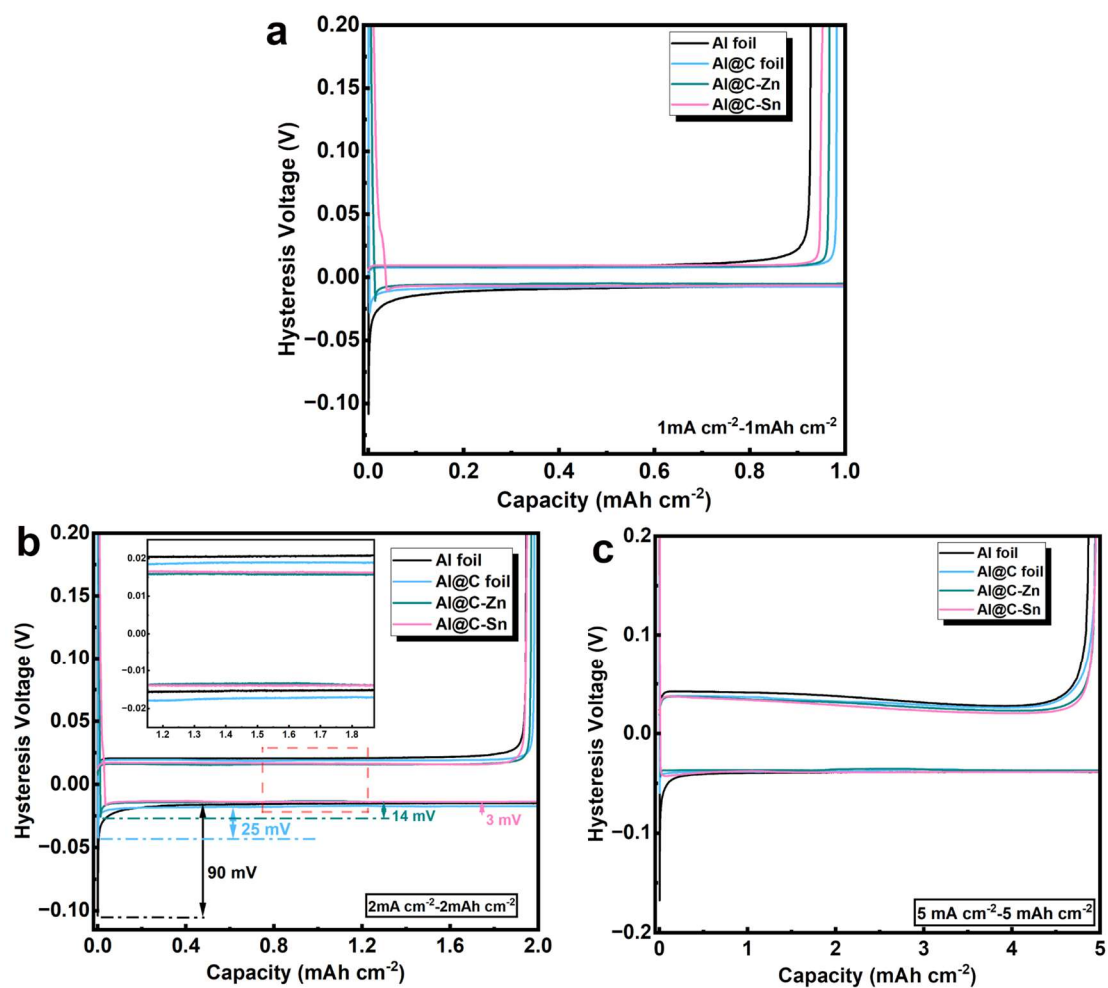
Figure S9. The Voltage-capacity curves of Na||Al foil, Na||Al@C foil, Na||Al@C-Zn and Na||Al@C-Sn half-cells at different current densities.
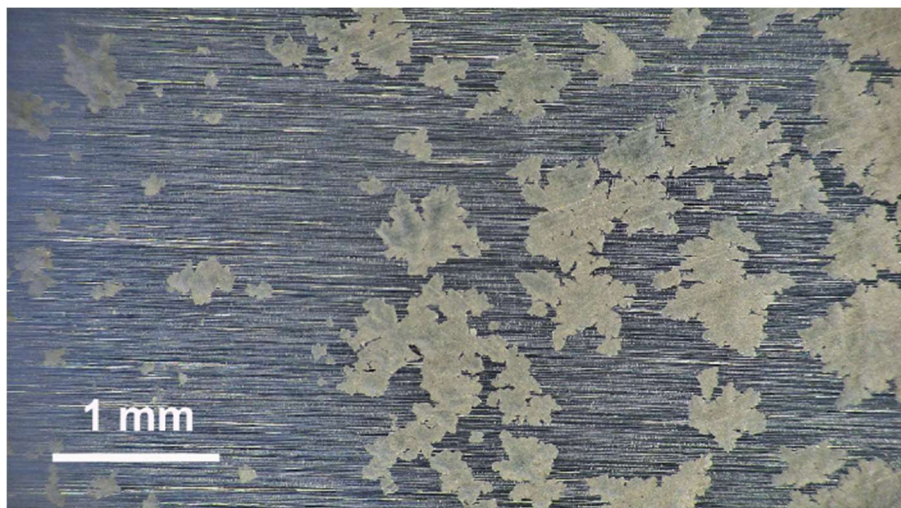
Figure S10. The optical image of Na deposition on Al foil in a half-cell at 2 mA cm^{-2} for 0.4 mAh cm^{-2}.
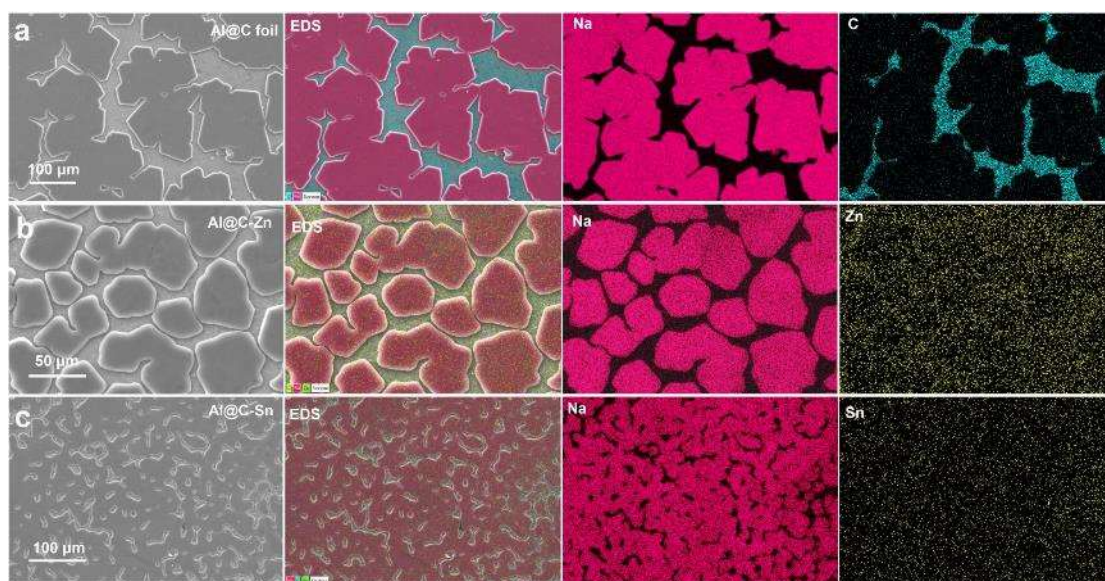
Figure S11. The SEM images and the corresponding EDS mappings of Na deposition on (a) Al@C foil, (b) Al@C-Zn and (c) Al@C-Sn in a half-cell at 2 mA cm^{-2} for 0.4 mAh cm^{-2}.
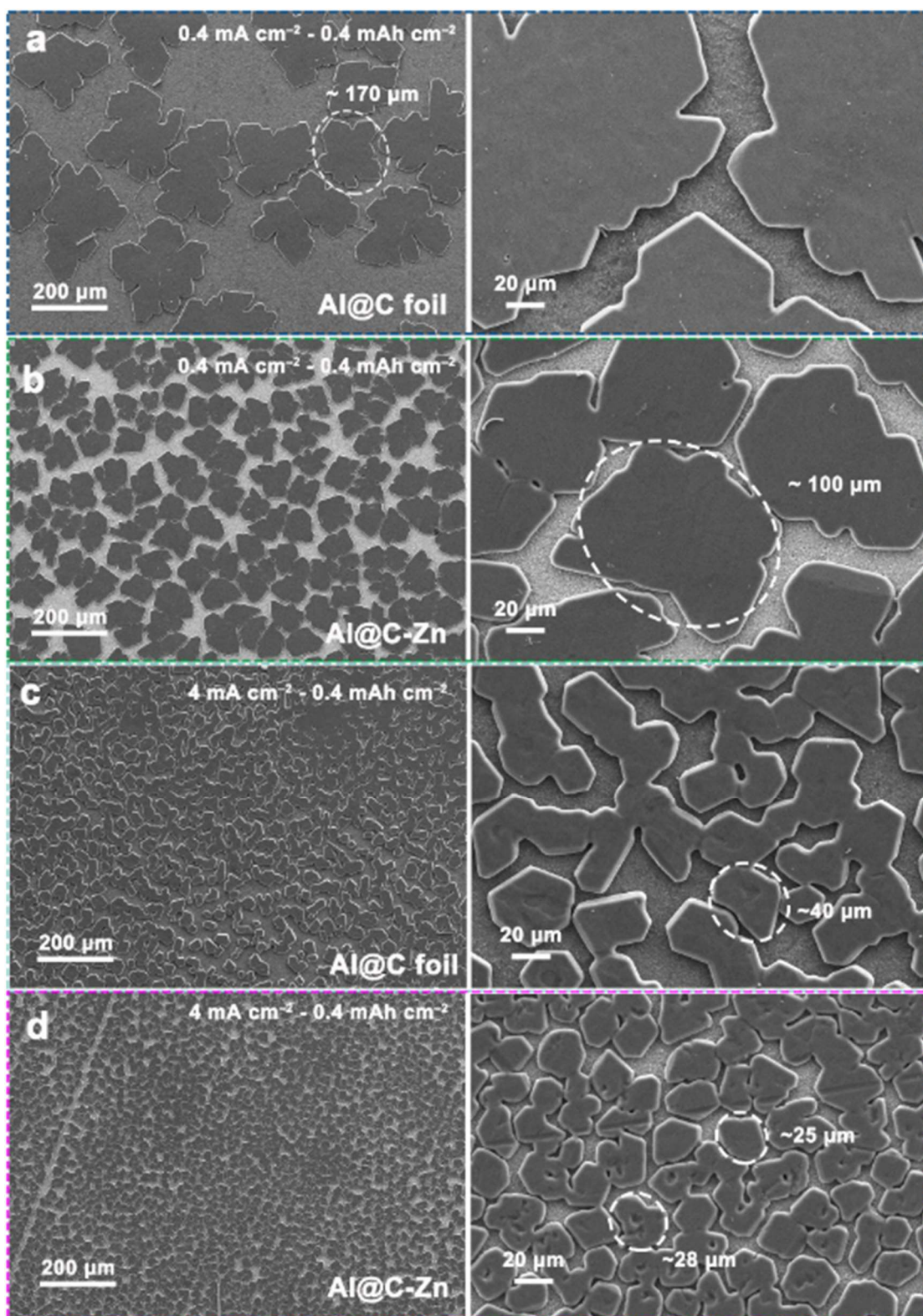
Figure S12. The deposition morphology of sodium on Al@C-Zn and Al@C foil at different current densities.
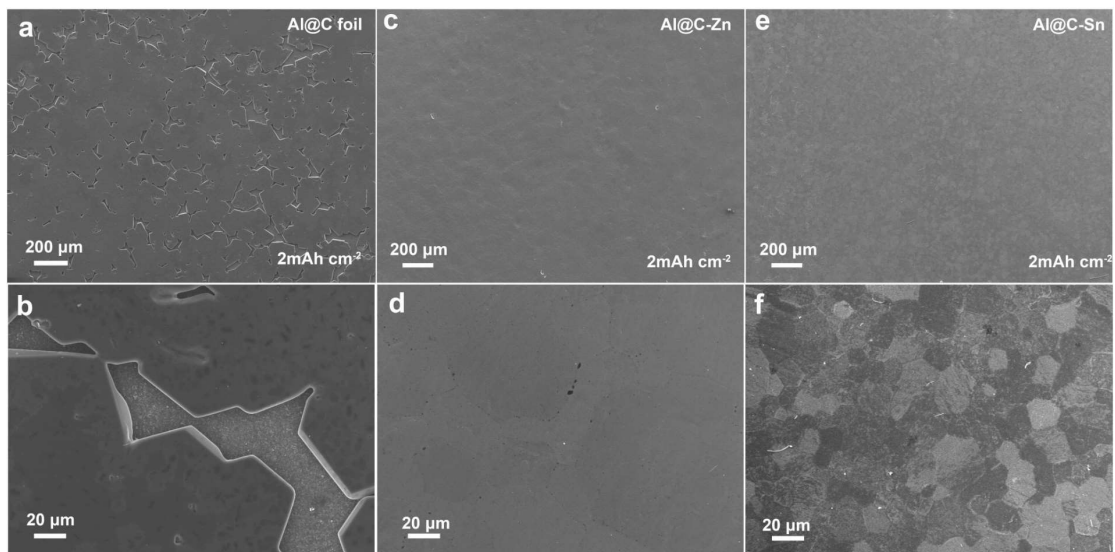
Figure S13. The SEM images of Na deposition on (a, b) Al@C foil, (c, d) Al@C-Zn and (e, f) Al@C-Sn in a half-cell at 2 mA cm^{-2} for 2 mAh cm^{-2}.
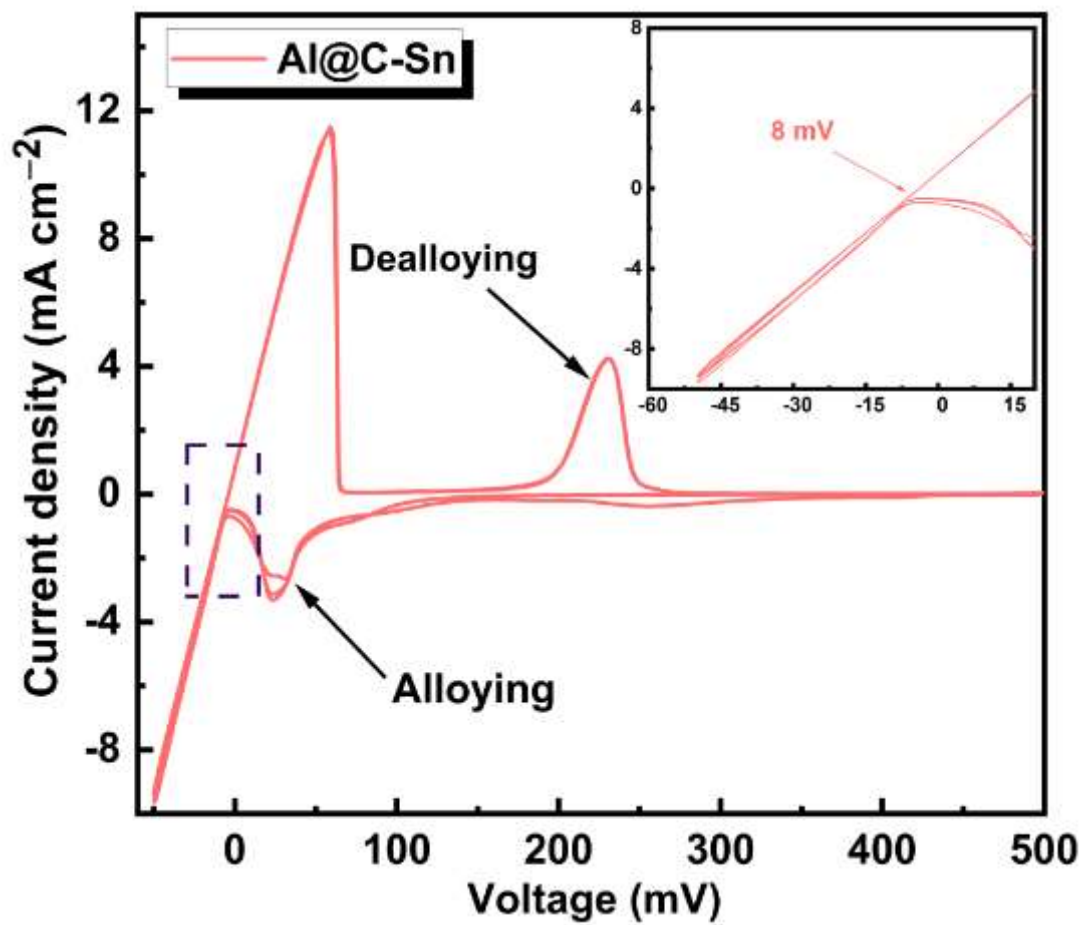
Figure S14. The CV curves of Na||Al@C-Sn half-cell at 1 mV s^{-1}.
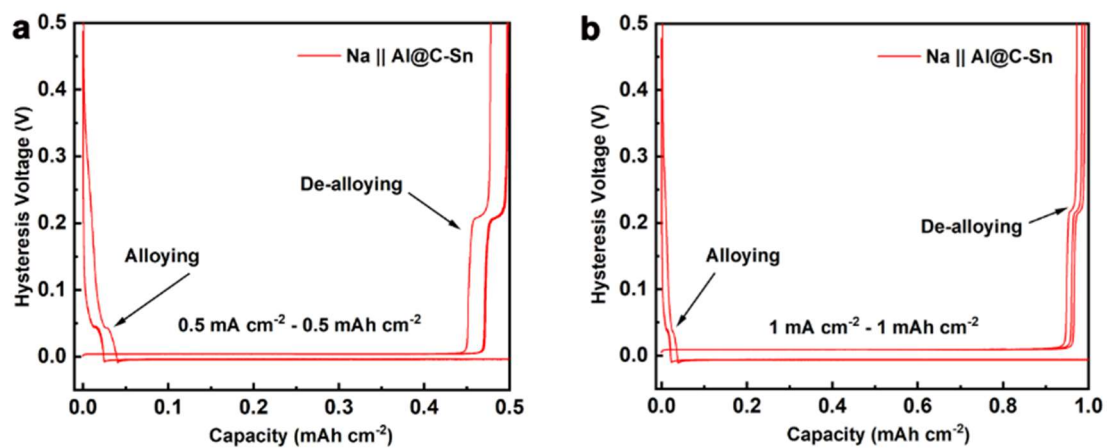
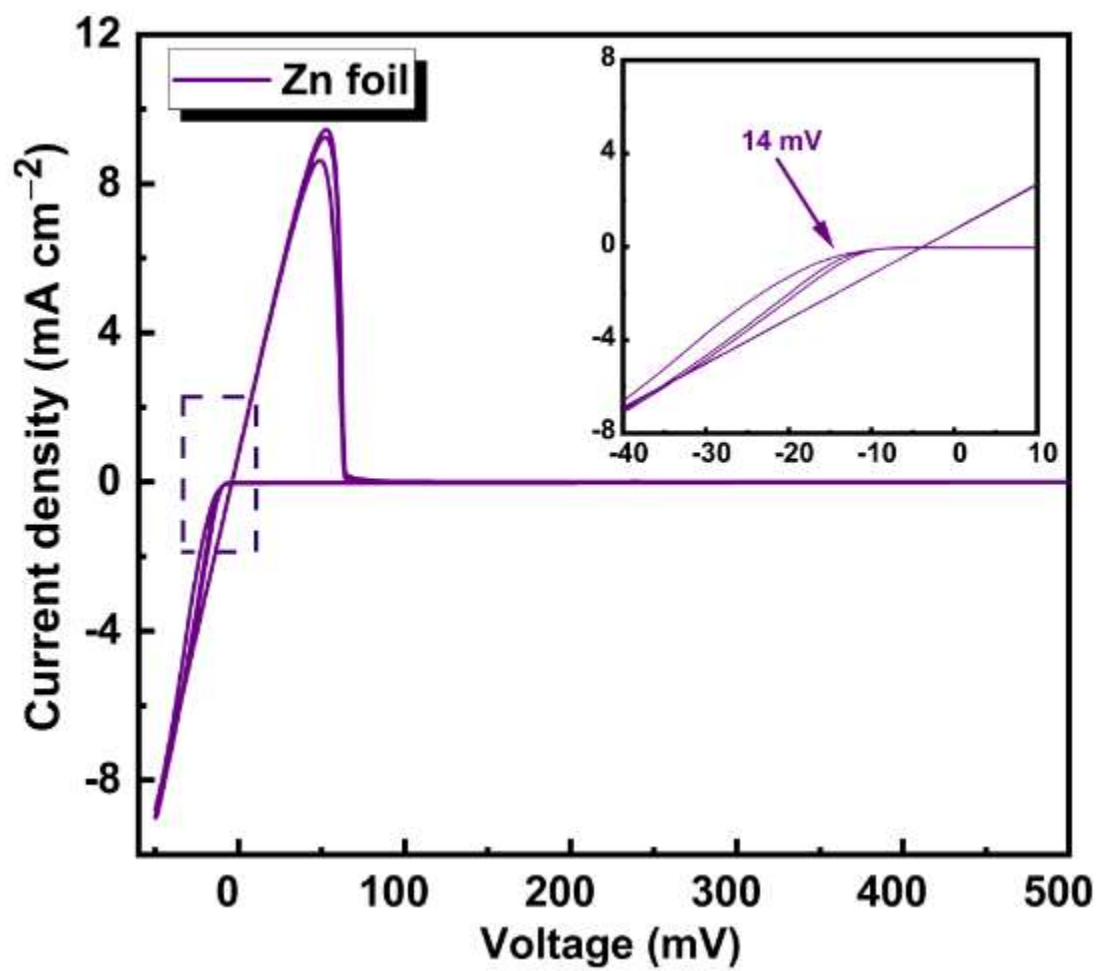**Figure S15.** The Voltage-capacity curves of Na‖Al@C-Sn half-cells at different current densities.

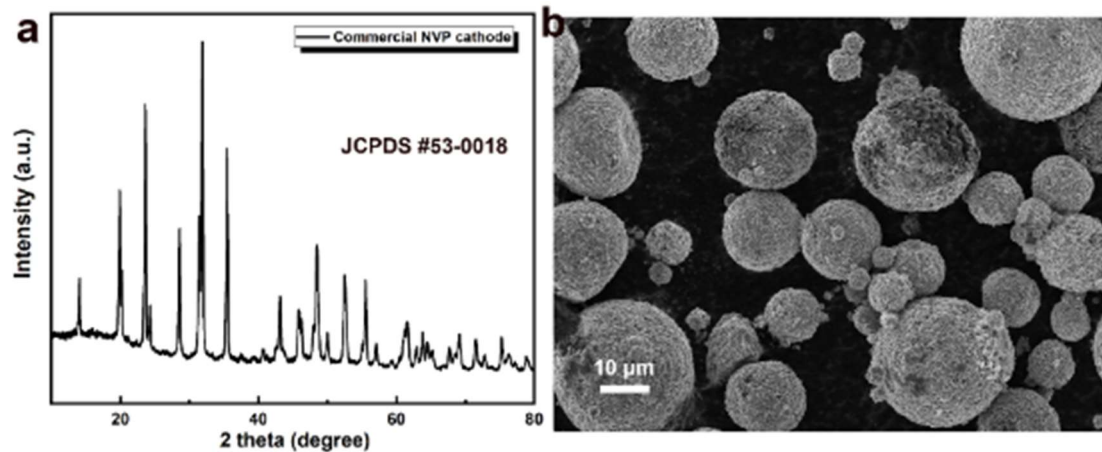**Figure S16.** The CV curve of Na||Zn foil half-cell at 1 mV s^{-1}.

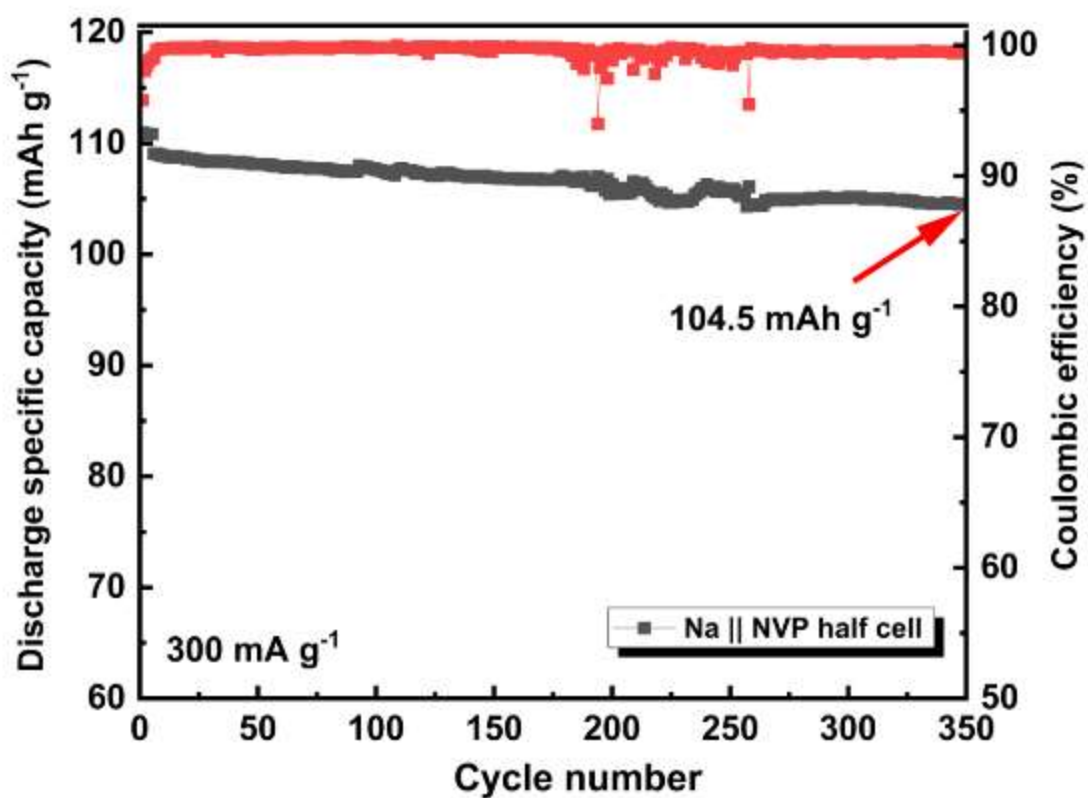**Figure S17.** The XRD pattern and SEM image of commercial $Na_3V_2(PO_4)_3$ cathode.

Figure S18. The cycling stability test of the Na||NVP cell (cathode loading is 10.1mg cm^{-2}).
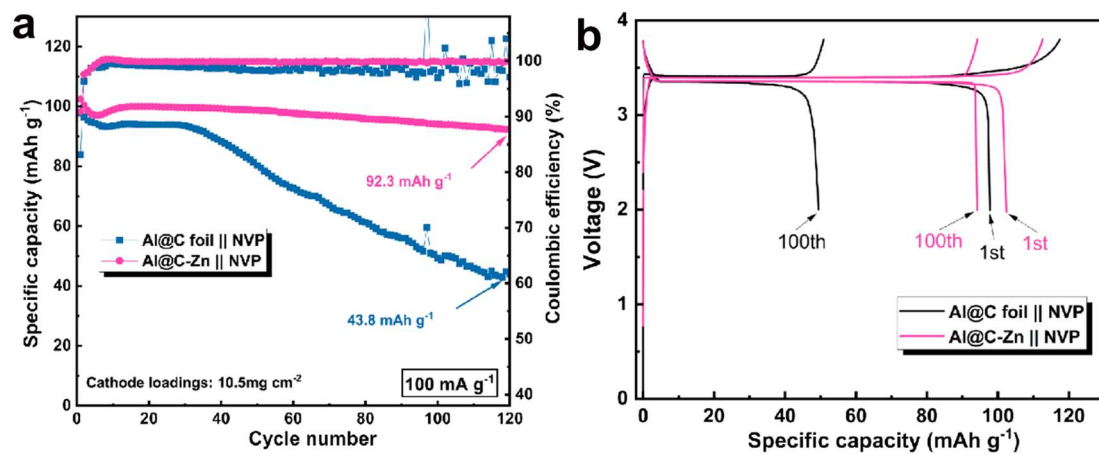
Figure S19. (a) Cycling stability curves and (b) capacity-voltage curves of Al@C‖NVP cell and Al@C-Zn‖NVP cell at 100 mA g^{-1} current density.
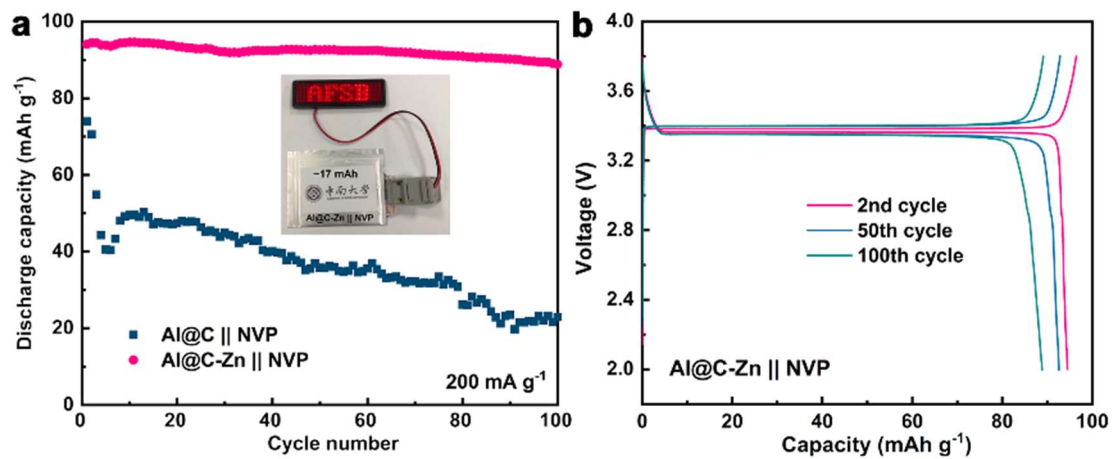
Figure S20. Cycling stability of pouch cells assembled with Al@C-Zn and Al@C foil.
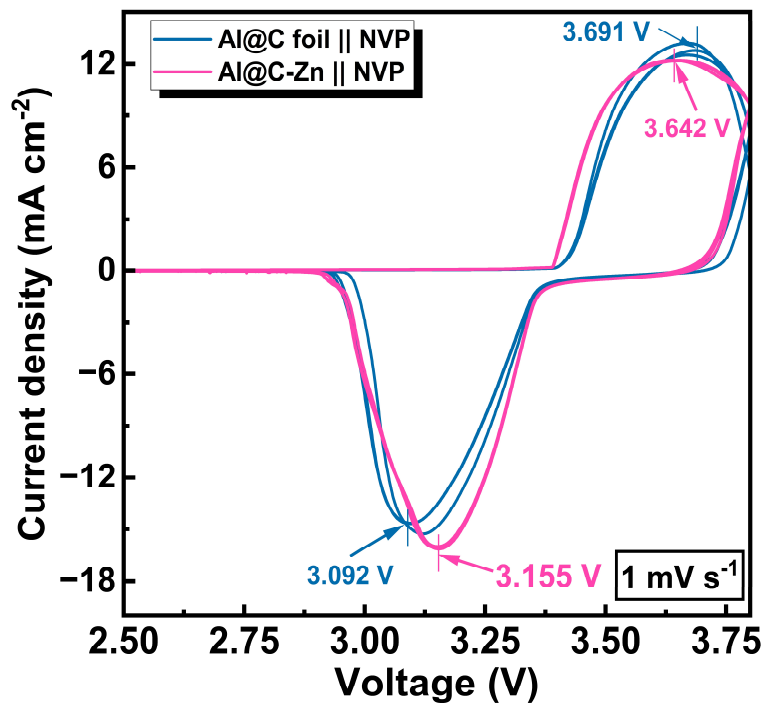
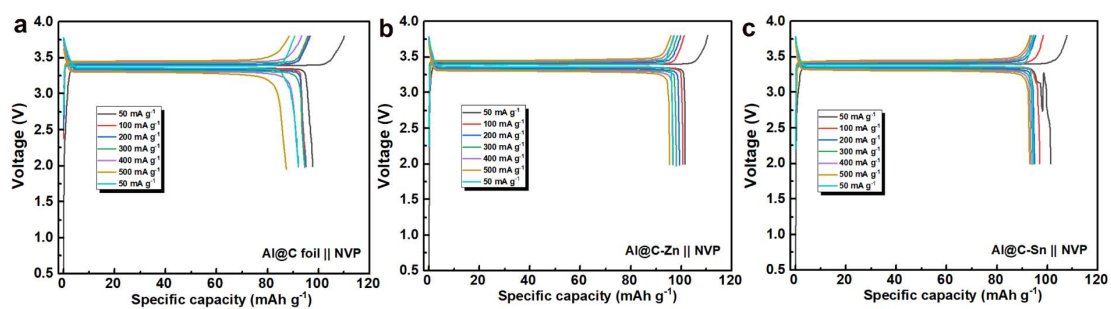**Figure S21.** The CV curves of Al@C||NVP cell and Al@C-Zn||NVP cell.

Figure S22. The capacity-voltage curves of Al@C||NVP cell, Al@C-Zn||NVP cell and Al@C-Sn||NVP cell at different current density.
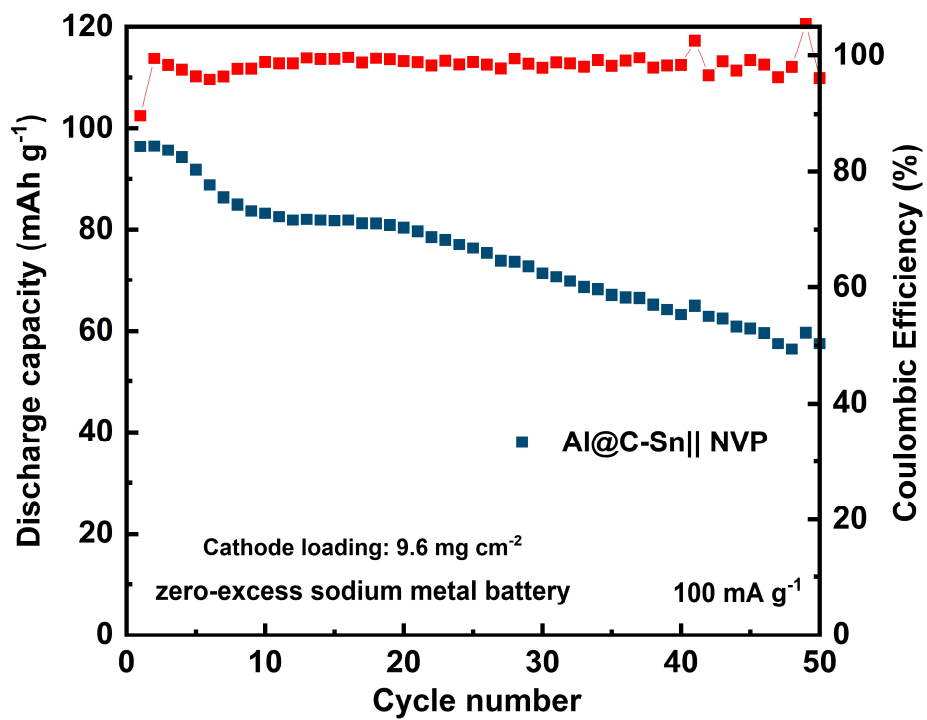
Figure S23. Cycling stability of Al@C-Sn||NVP cell at 100 mA g^{-1} current density (Sn was sputtered on Al@C foil substrate for 3min at 100W power).
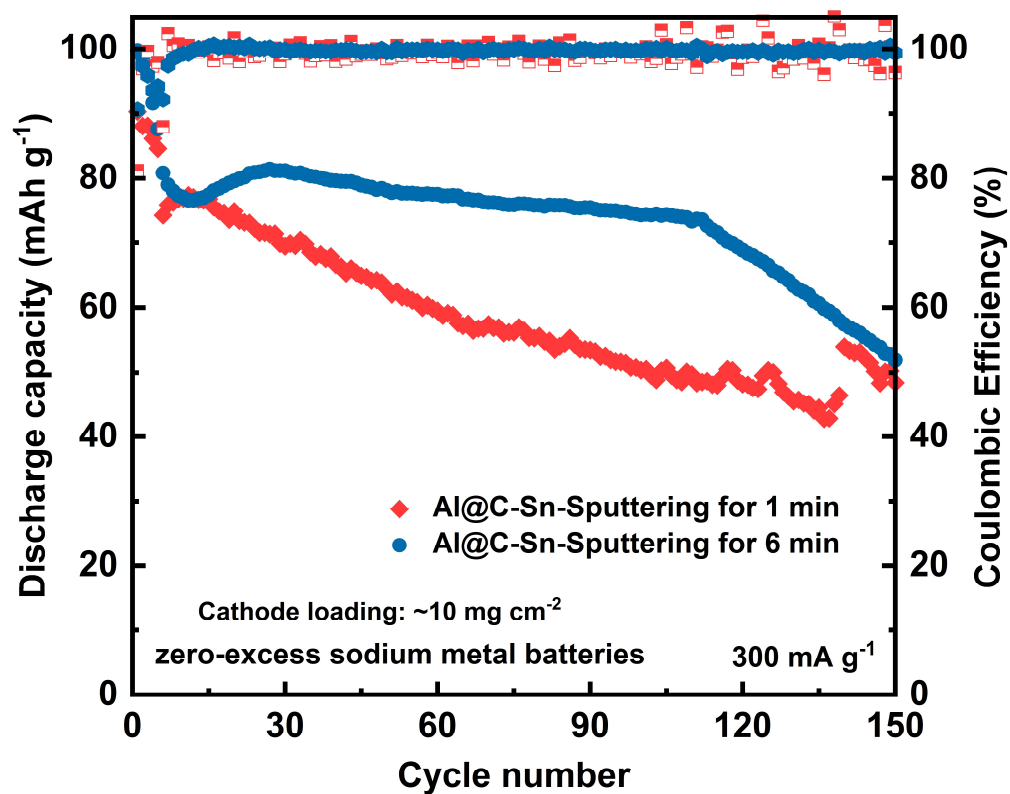
Figure S24. Full-cell cycle stability of Al@C-Sn prepared by magnetron sputtering for different time.
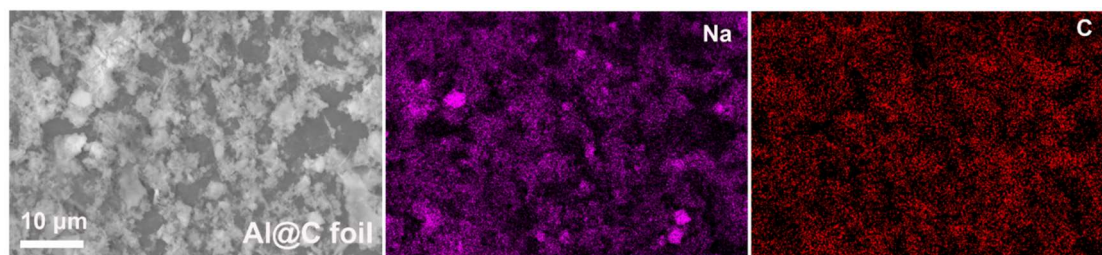
Figure S25. Anode-side SEM images and corresponding EDS mappings of Al@C ||NVP cell after 100 cycles at 300 mA g^{-1} in a fully discharged state.
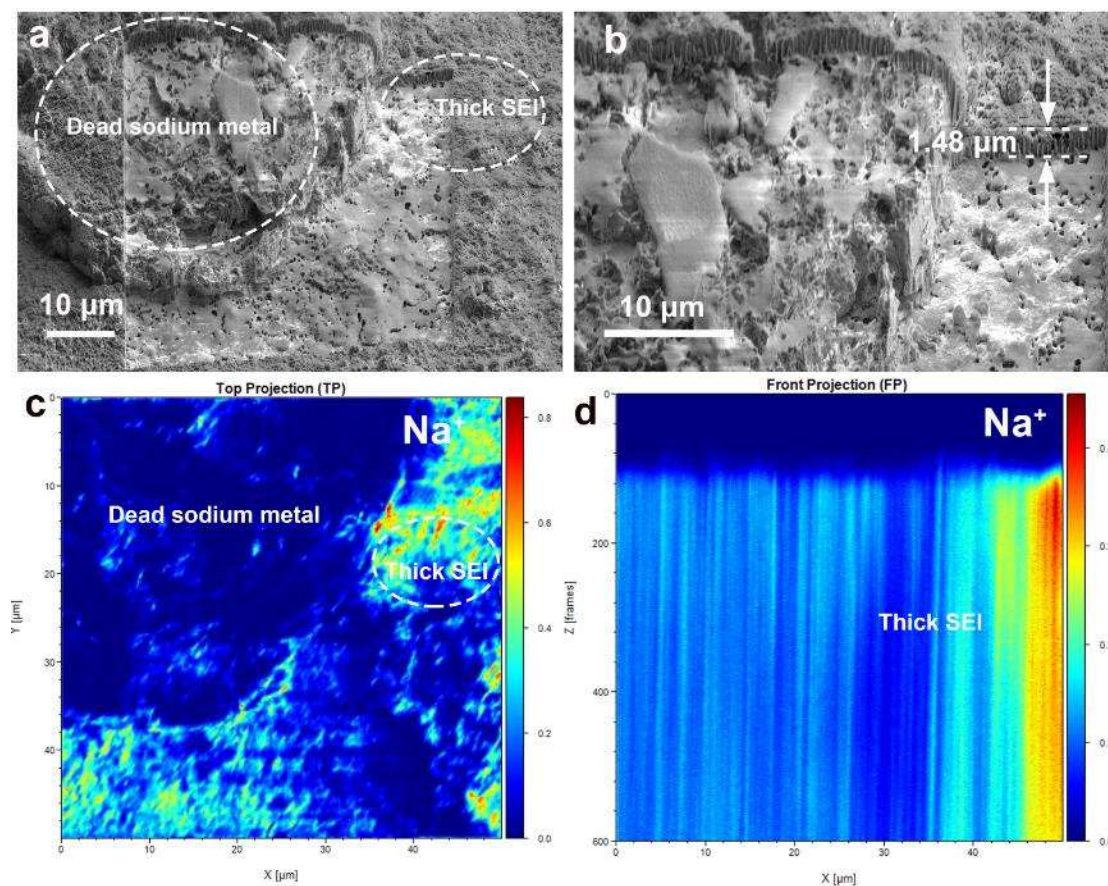
Figure S26. (a, b) Anode-side SEM images after Ga-ion processing (positive ion detection) of Al@C‖NVP cell, after 100 cycles at 300 mA g^{-1} in a fully discharged state. (c) Top-view and (d) depth-view TOF-SIMS of the Na$^+$ in the square region in Figure S26a.

The inactive sodium is sodium in zero valence state, which generates almost no ionic fragments after bombardment by gallium ions and thus cannot be recognized by the TOF-SIMS detector, so inactive sodium cannot be recognized by TOF-SIMS. But the presence of inactive sodium can be determined from SEM images combined with EDS. Thus, the protruding portion in Figure S26, which has no apparent sodium ion signal, can be judged to be inactive sodium rather than SEI.
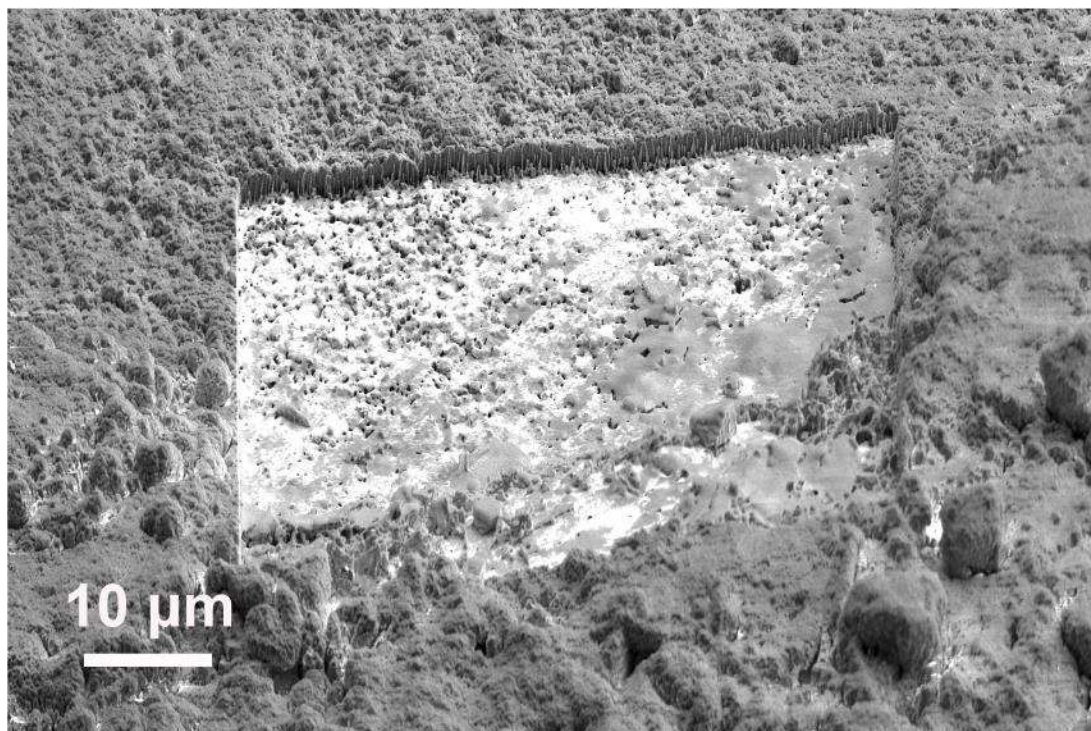
Figure S27. Anode-side SEM images after Ga-ion processing (negative ion detection) of Al@C‖NVP cell, after 100 cycles at 300 mA g^{-1} in a fully discharged state.
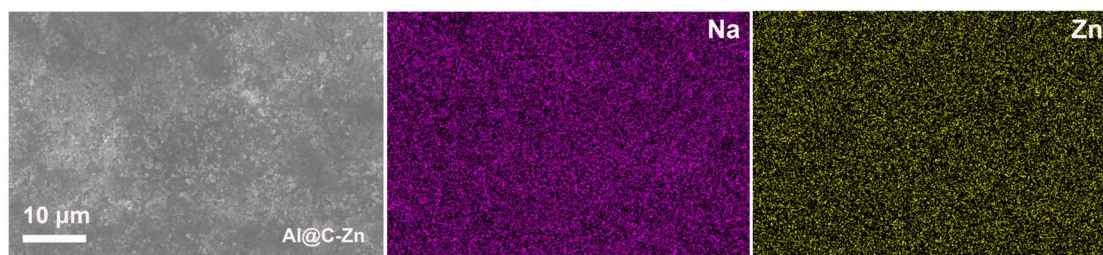
Figure S28. Anode-side SEM images and corresponding EDS mappings of Al@C-Zn||NVP cell after 100 cycles at 300 mA g^{-1} in a fully discharged state.

Figure S29. (a, b) Anode-side SEM images after Ga-ion processing (negative ion detection) of Al@C-Zn‖NVP cell, after 100 cycles at 300 mA g^{-1} in a fully discharged state.

Figure S30. TOF-SIMS of P and B components of Al@C-Zn substrates after 100 cycles at 300 mA g^{-1} in a fully discharged state.

Figure S31. TOF-SIMS of P and B components of Al@C foil substrates after 100 cycles at 300 mA g^{-1} in a fully discharged state.

Figure S32. (a, b) Anode-side SEM image and EDSs of Al@C-Sn‖NVP cell, after 100 cycles at 300 mA g^{-1} in a fully discharged state.
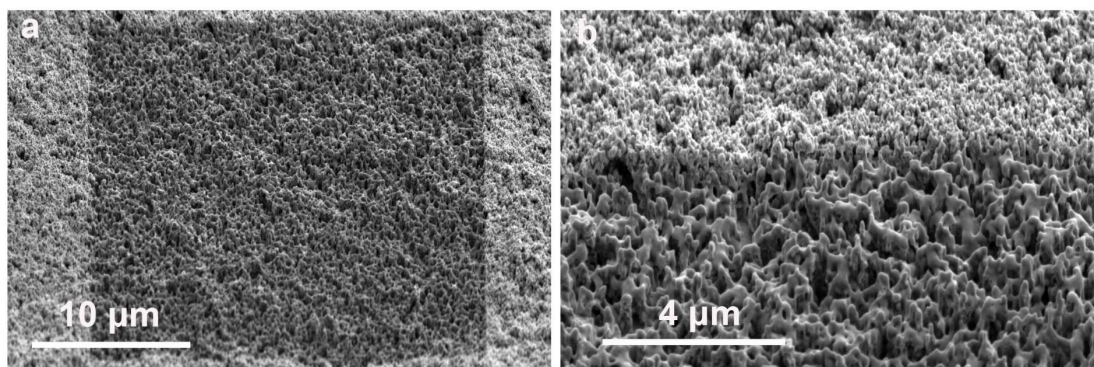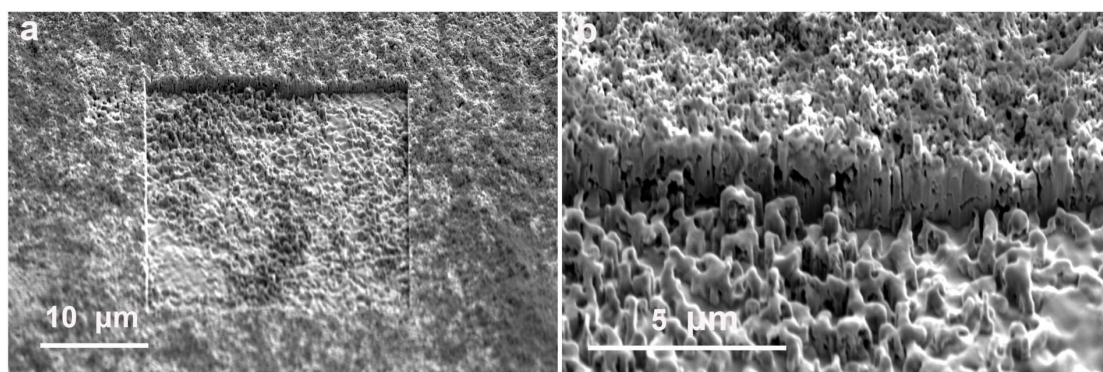
Figure S33. (a, b) Anode-side SEM images after Ga-ion processing (negative ion detection) of Al@C-Sn‖NVP cell, after 100 cycles at 300 mA g^{-1} in a fully discharged state.
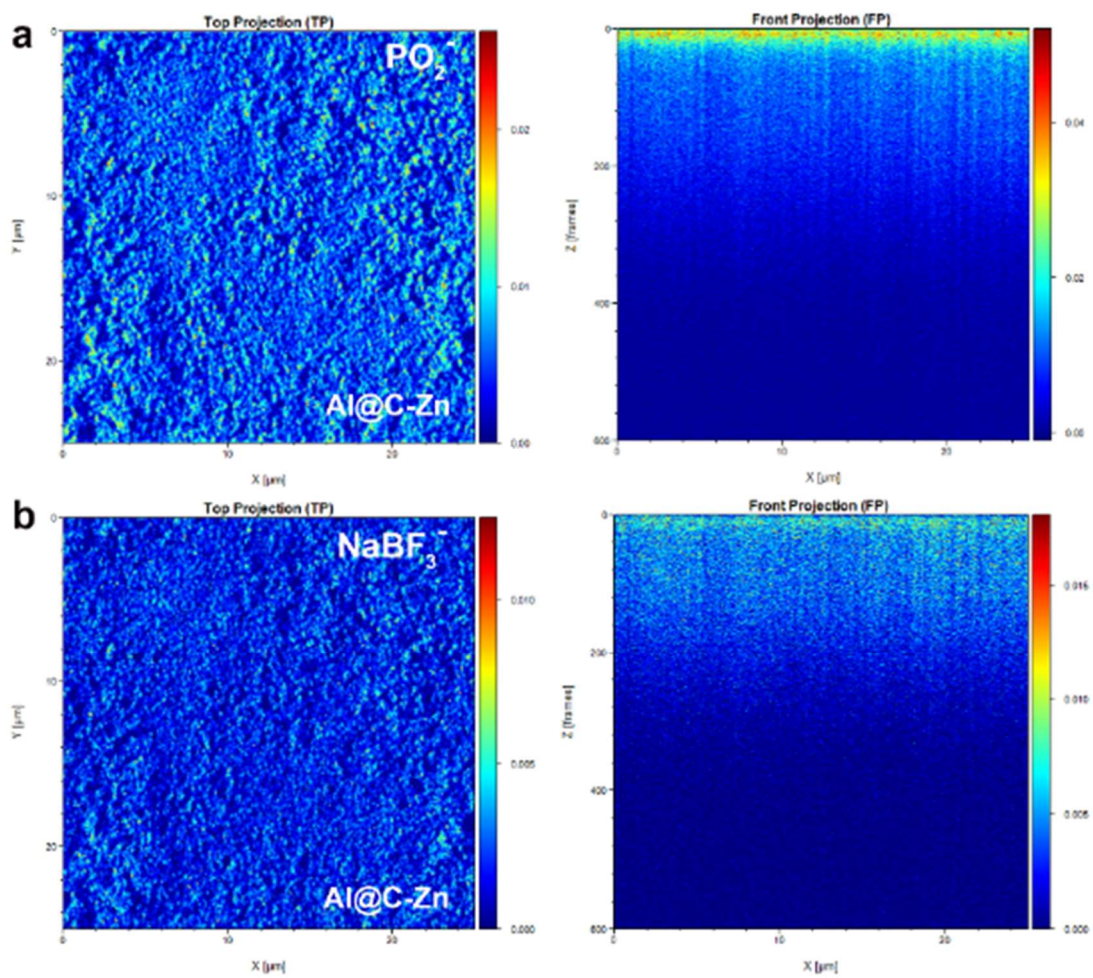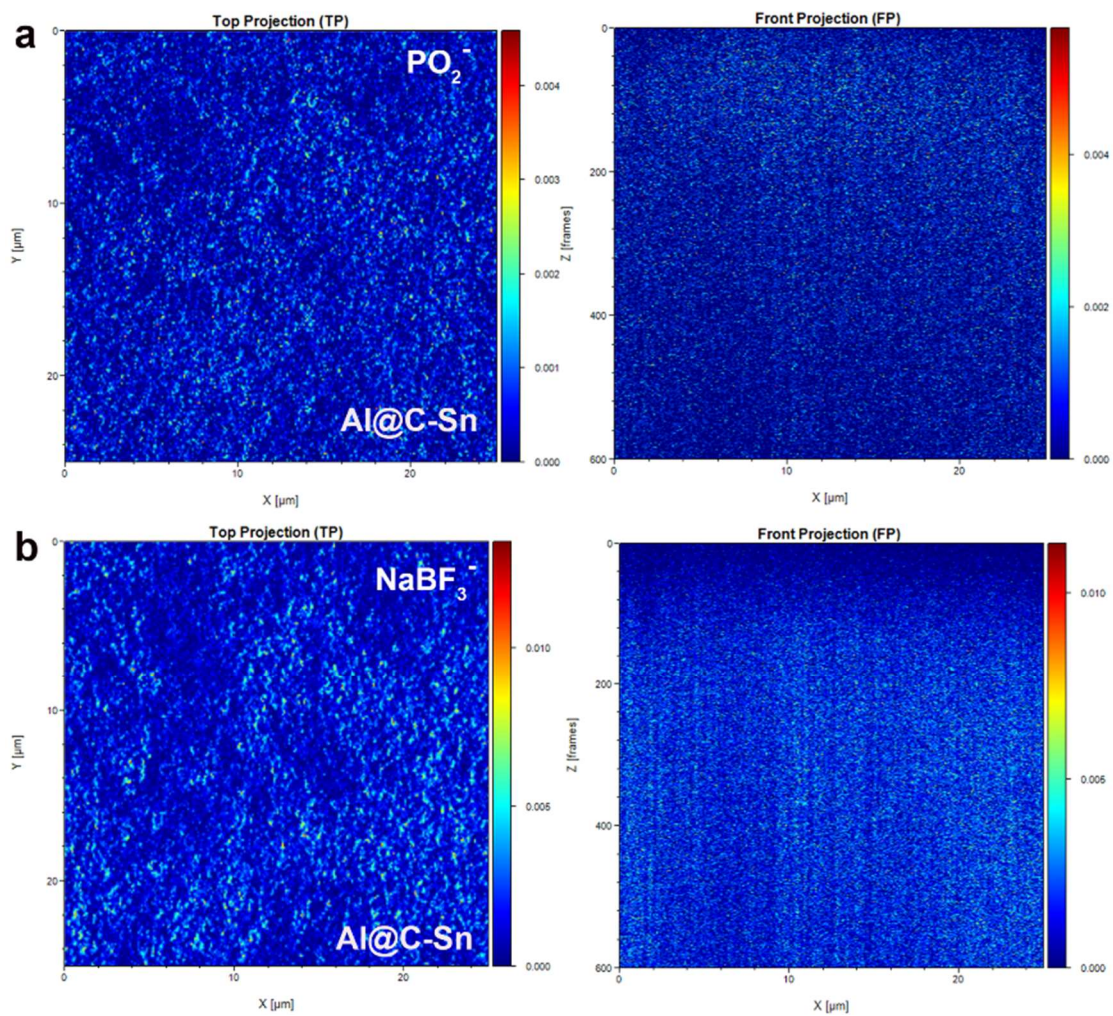
Figure S34. TOF-SIMS of P and B components of Al@C-Sn substrates after 100 cycles at 300 mA g^{-1} in a fully discharged state.
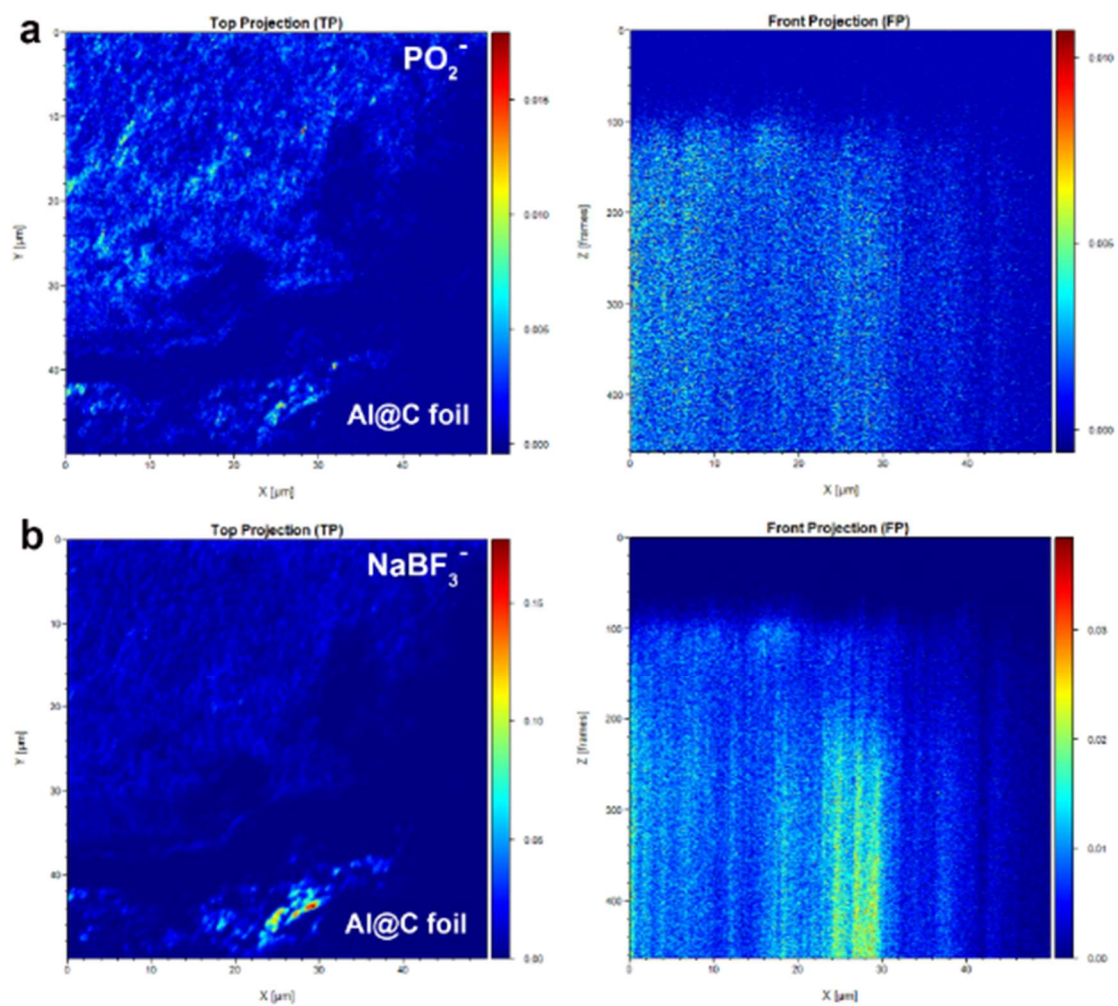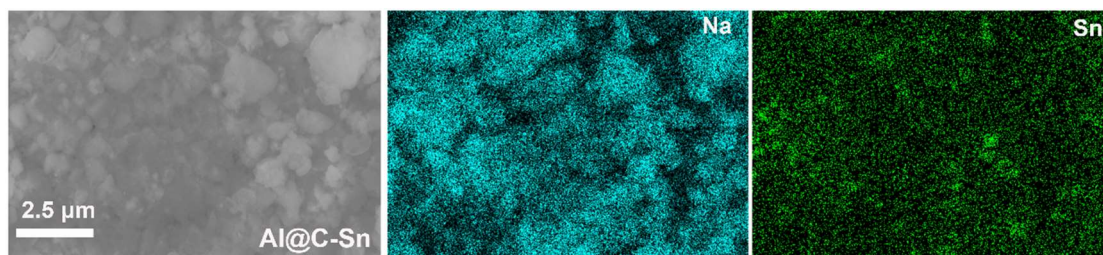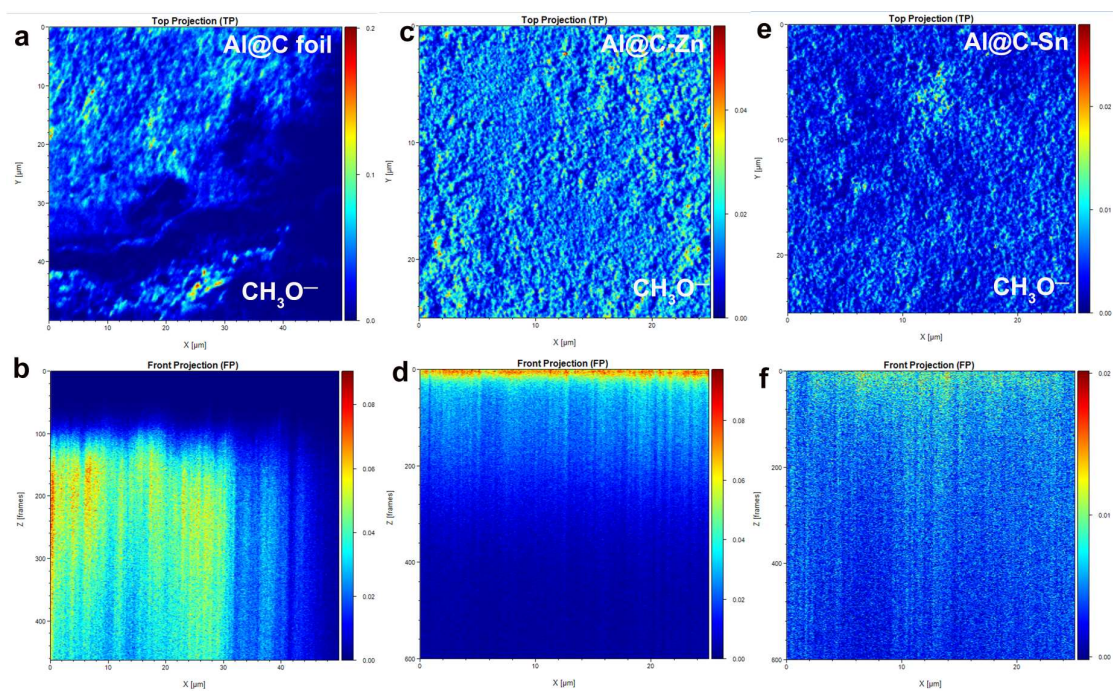
Figure S35. TOF-SIMS of CH_3O^- organic components of different substrates after 100 cycles at 300 mA g^1 in a fully discharged state.
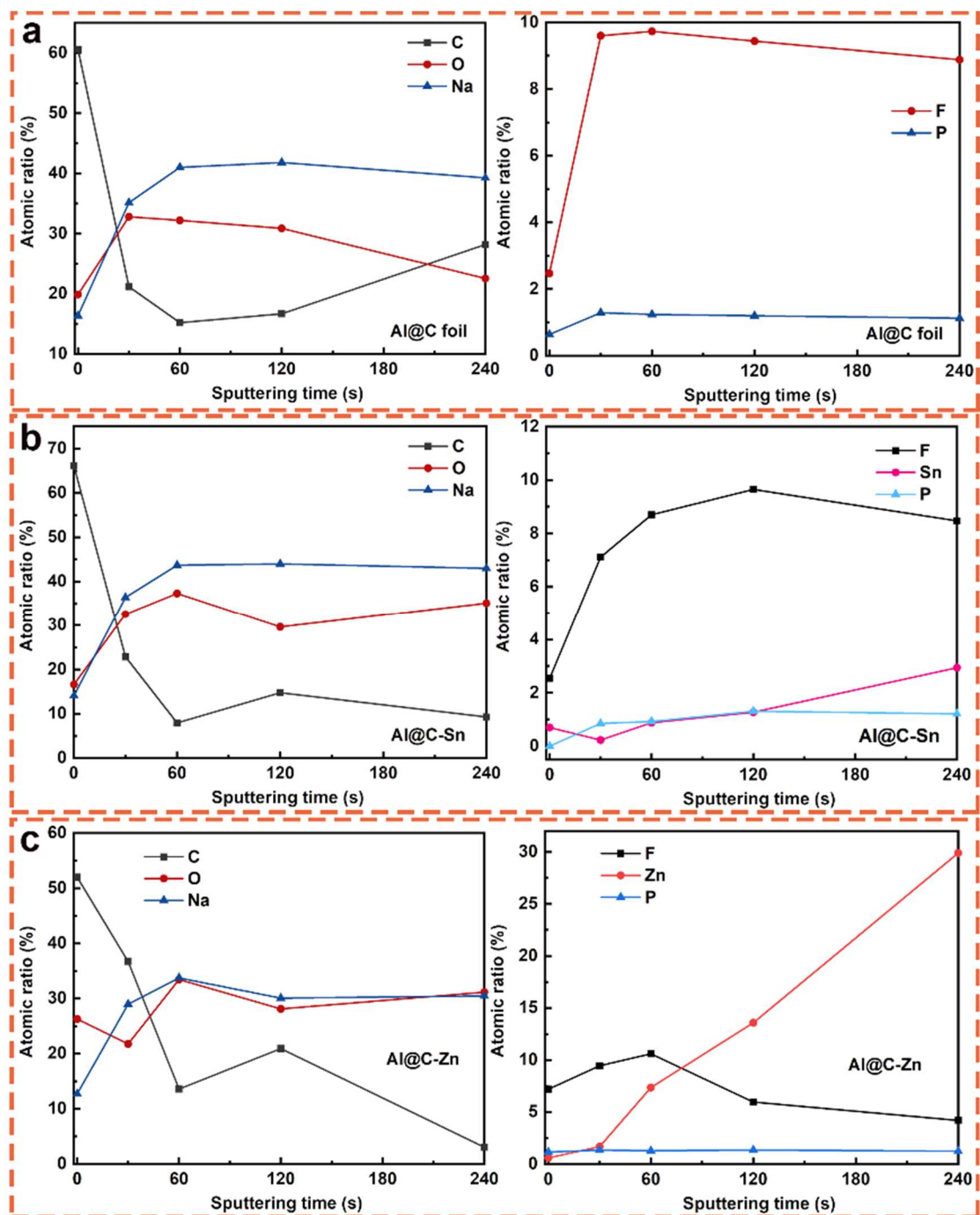
Figure S36. Elemental content variation trends of (a) Al@C foil, (b) Al@C-Sn and (c) Al@C-Zn substrates at different etching depths after 100 cycles at 300 mA g^{-1} in a fully discharged state.

Figure S37. XPS of F1s spectra of Al@C foil, Al@C-Sn and Al@C-Zn substrates with different etching depths.

Figure S38. XPS of C1s spectra of Al@C foil, Al@C-Sn and Al@C-Zn substrates with different etching depths.

Figure S36c shows that element F, an important component in SEI, increases and then decreases in content as etching depth increases for Al@C-Zn substrate. After 240s of etching, the content of element F decreases to 4.2%. This suggests that element F is

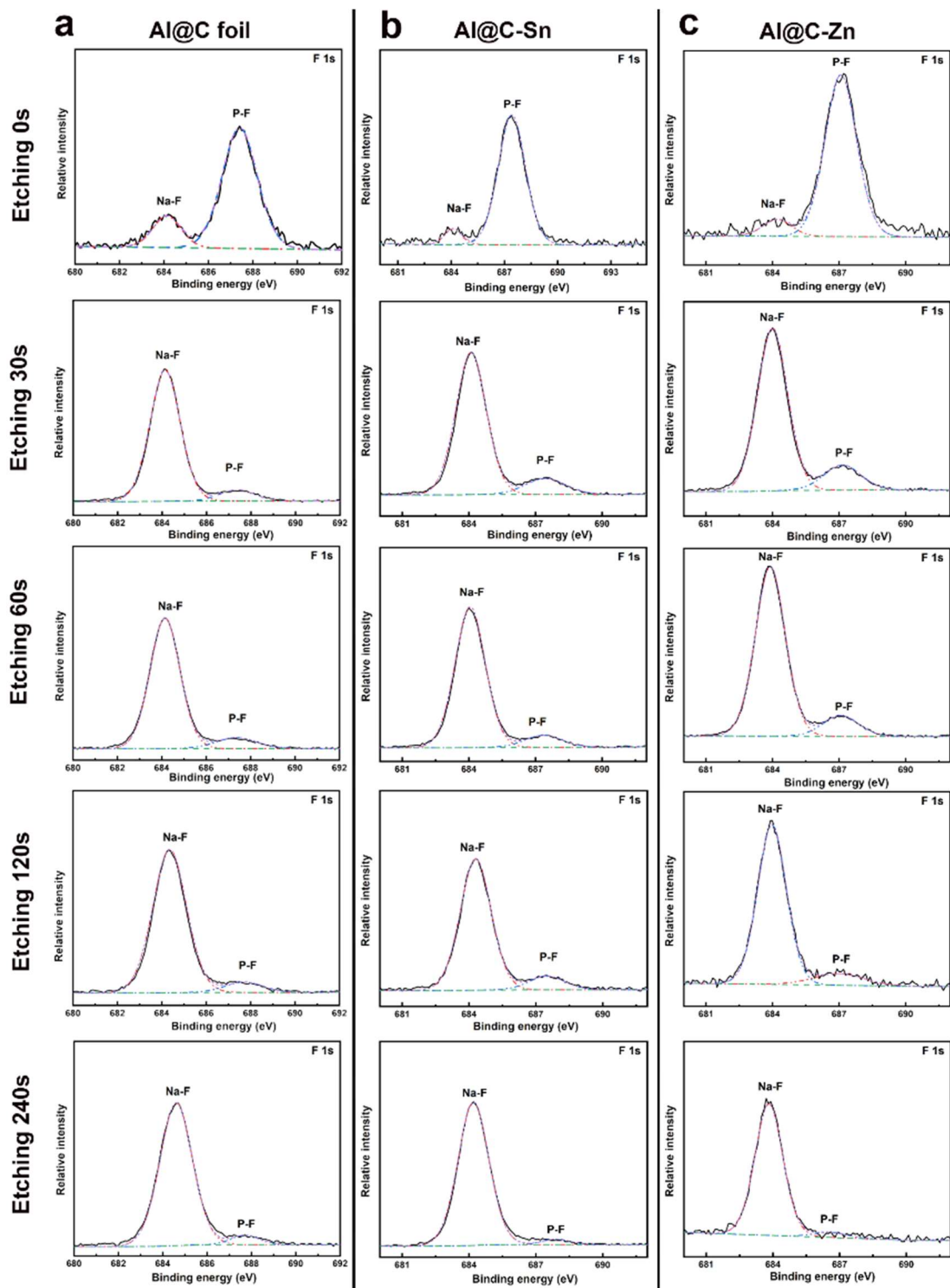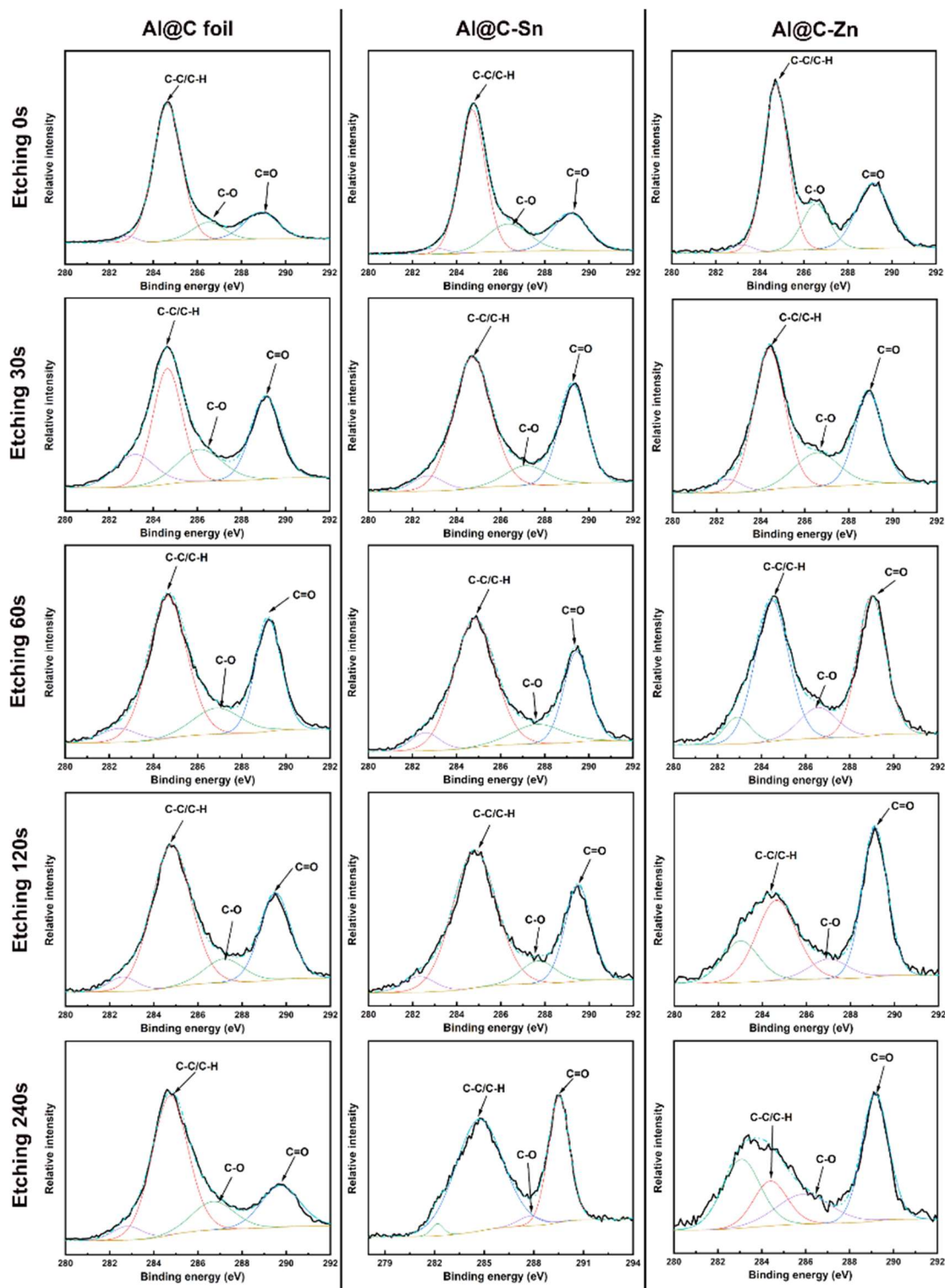enriched at shallow surfaces and then significantly decreases at deeper surfaces, which is consistent with the depth distribution regularity of F^- shown in Figure 4g. As the depth of the etching increases, the amount of elemental carbon decreases, and the zinc elements become gradually exposed (Figure S36c). In contrast, the Sn element increases only slowly with etching depth for the structurally unstable Al@C-Sn substrate, while there is no significant decreasing trend for the fluorine element (Figure S36b). For Al@C foil (Figure S36a), it was also observed that the concentration of fluorine did not decrease significantly with increasing etching depth. This suggests that a thick SEI was formed on the surface of Al@C foil. The XPS spectra of the F1s also show that the elements F at the substrate interface are predominantly in the form of NaF, except for a small amount of P-F components in the outermost layers (Figure S37). The XPS spectra of C1s show an organic C-O component on the surface of the Al@C-Zn substrate (Figure S38).[1] The organic component decreases significantly with increasing etching depth and carbon content. This indicates that the Al@C-Zn substrate forms a SEI with a thin organic component, which exhibits a similar pattern to the distribution of the organic component of the CH_3O^- from TOF-SIMS (Figure S35).
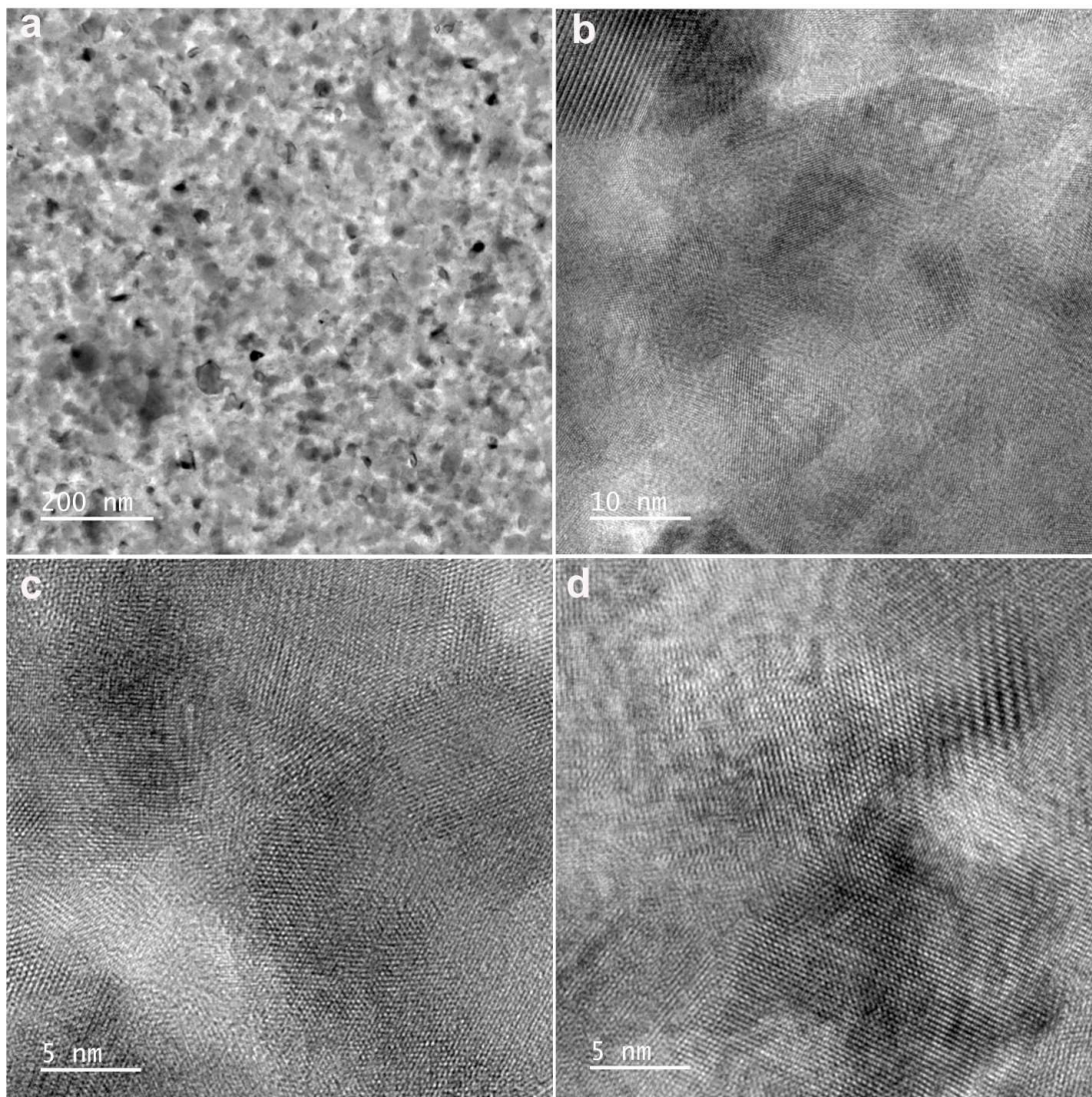
Figure S39. TEM images of zinc layer on molybdenum mesh after 5 cycles of sodium plating/stripping (in the stripped state).

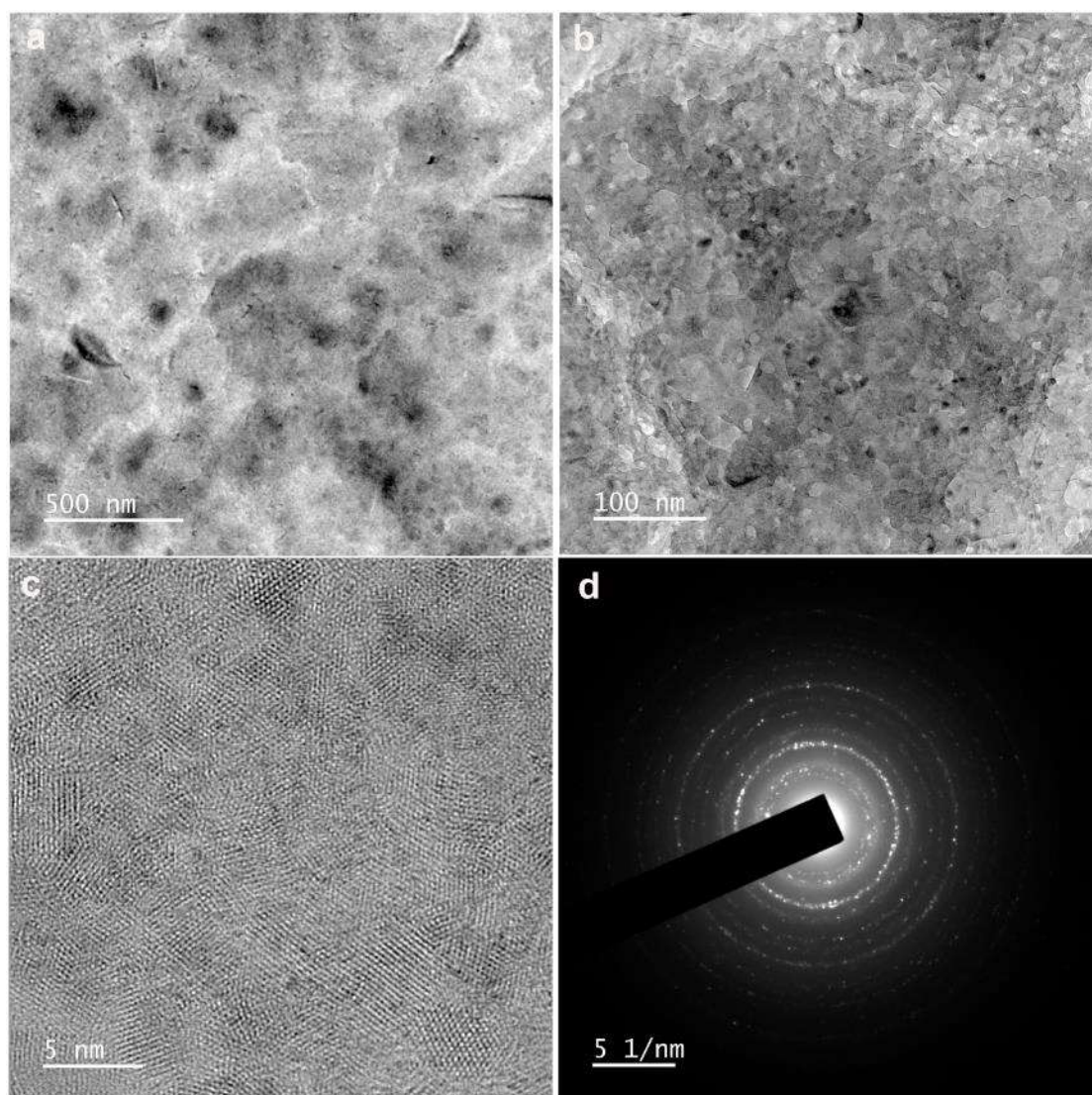**Figure S40.** (a-c) TEM images and (d) electron diffraction pattern of zinc layer on molybdenum mesh after 50 cycles of sodium plating/stripping (in the stripped state).
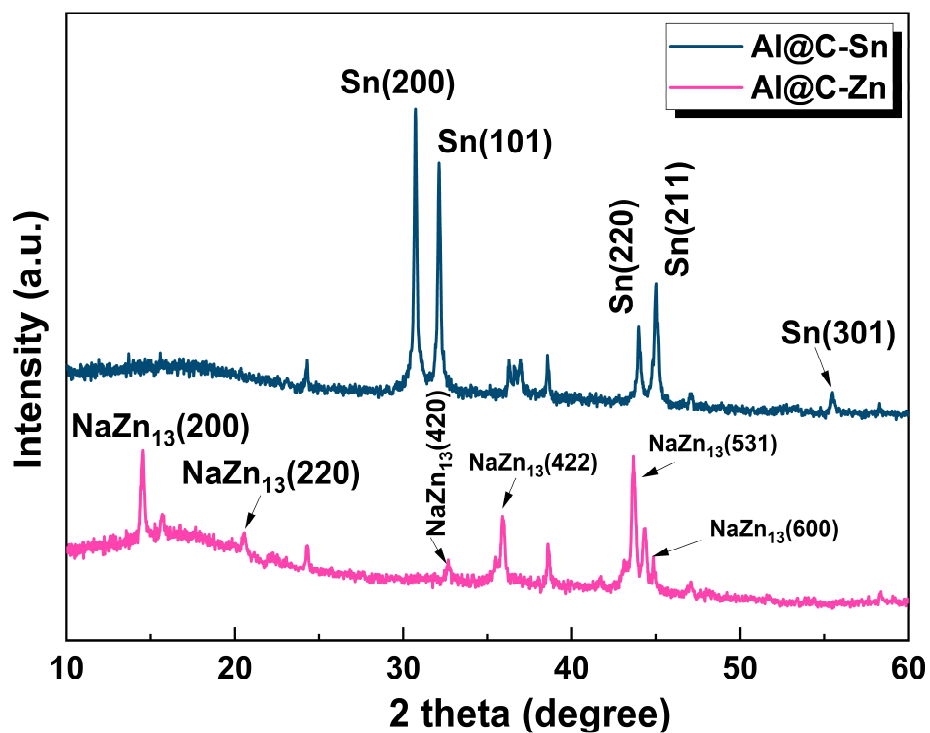
Figure S41. XRD patterns of Al@C-Sn and Al@C-Zn substrates after 5 cycles in a half-cell at 2 mA cm^{-2} for 2 mAh cm^{-2} in a fully stripping state.

Figure S42. The cycling stability of Zn foil||NVP cell at 300 mA g^{-1}.

Map Sum Spectrum			
Element	Wt%	Wt% Sigma	Atomic %
O	7.35	0.11	15.79
F	14.65	0.12	26.49
Na	5.74	0.19	8.59
P	19.12	0.10	21.21
Zn	53.14	0.18	27.93
Total:	100.00		100.00
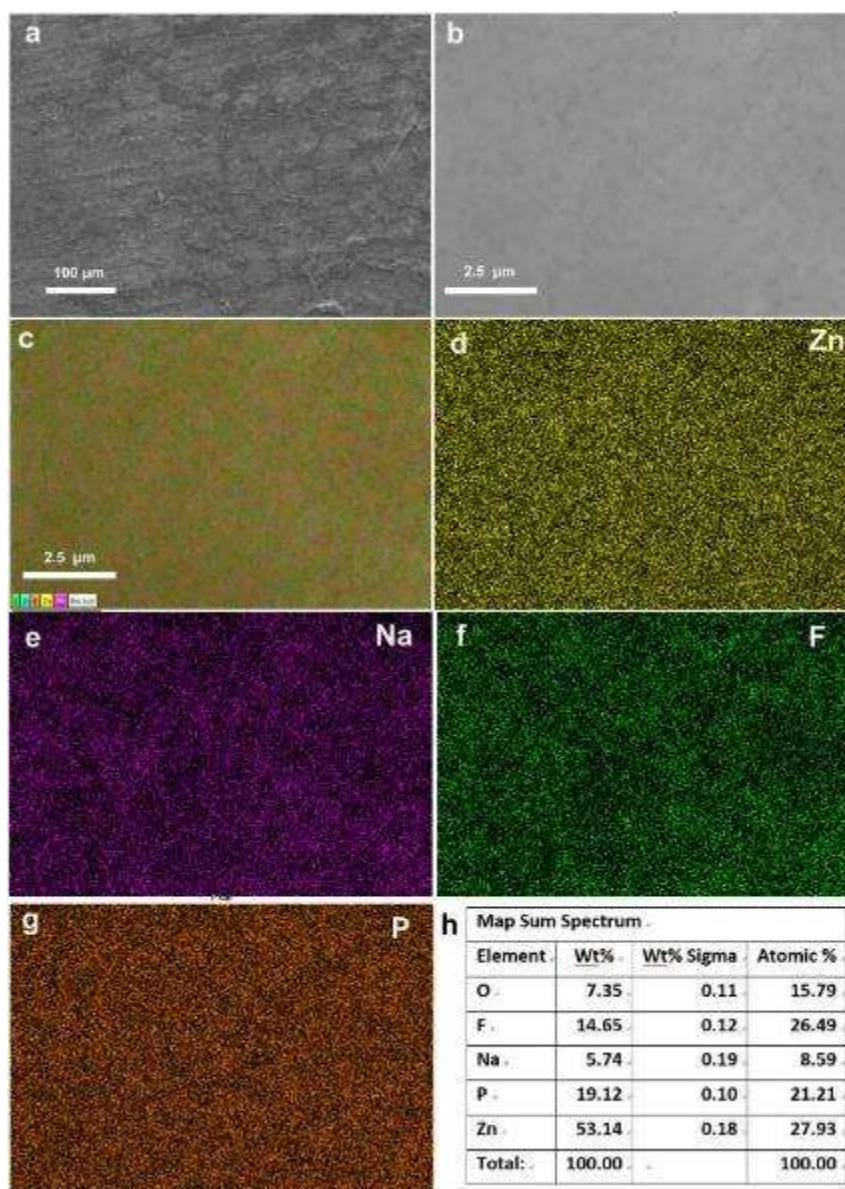
Figure S43. Anode-side SEM images and corresponding EDS mappings of Zn foil‖NVP cell after 5 cycles at 300 mA g^{-1} in a fully discharged state.
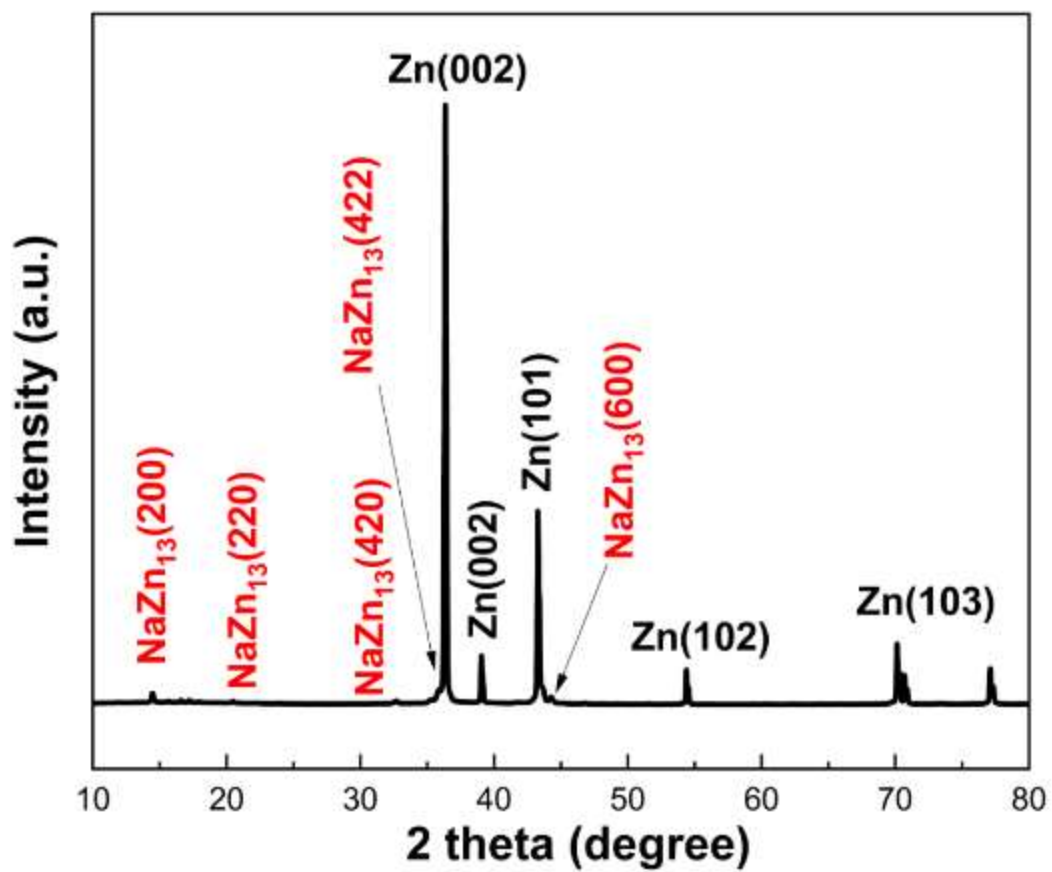
Figure S44. The XRD pattern of zinc foil substrates after 5 cycles in a half-cell at 2 mA cm^{-2}–2 mAh cm^{-2} in a fully stripping state.

Element	Atomic %
Na	55.93
Sn	44.07
Total:	100.00
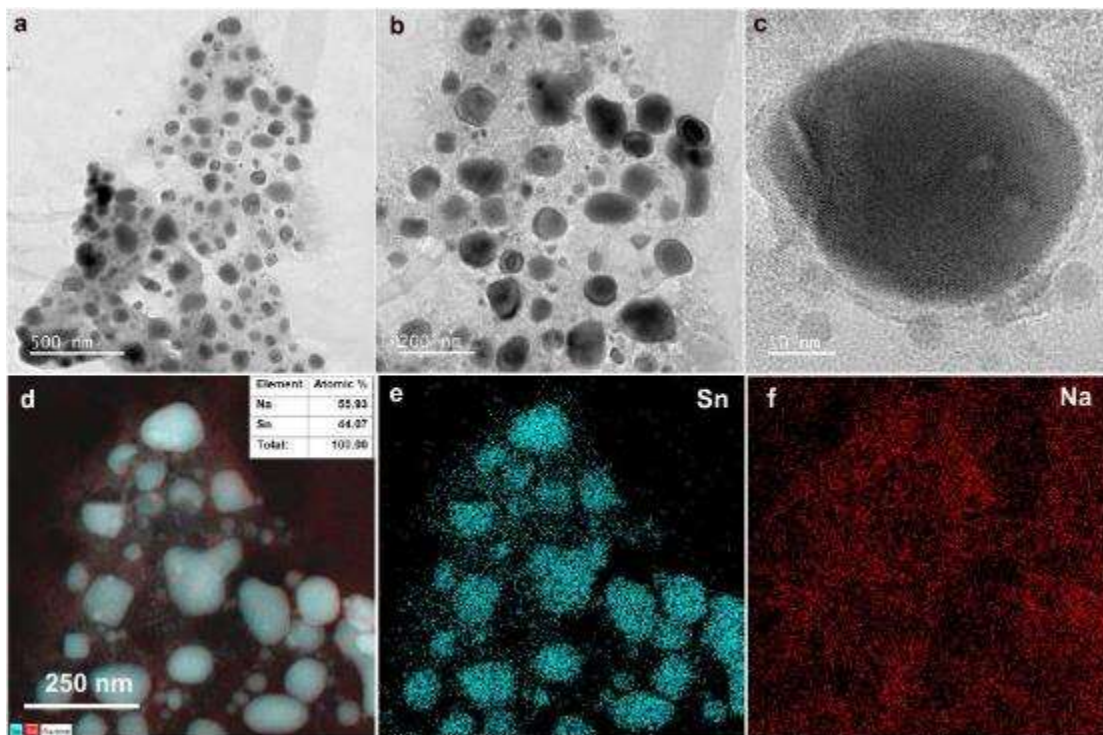
Figure S45. (a-c) TEM images and (d-f) corresponding EDS mappings of tin layer on molybdenum mesh after 50 cycles of sodium plating/stripping (in the stripped state).
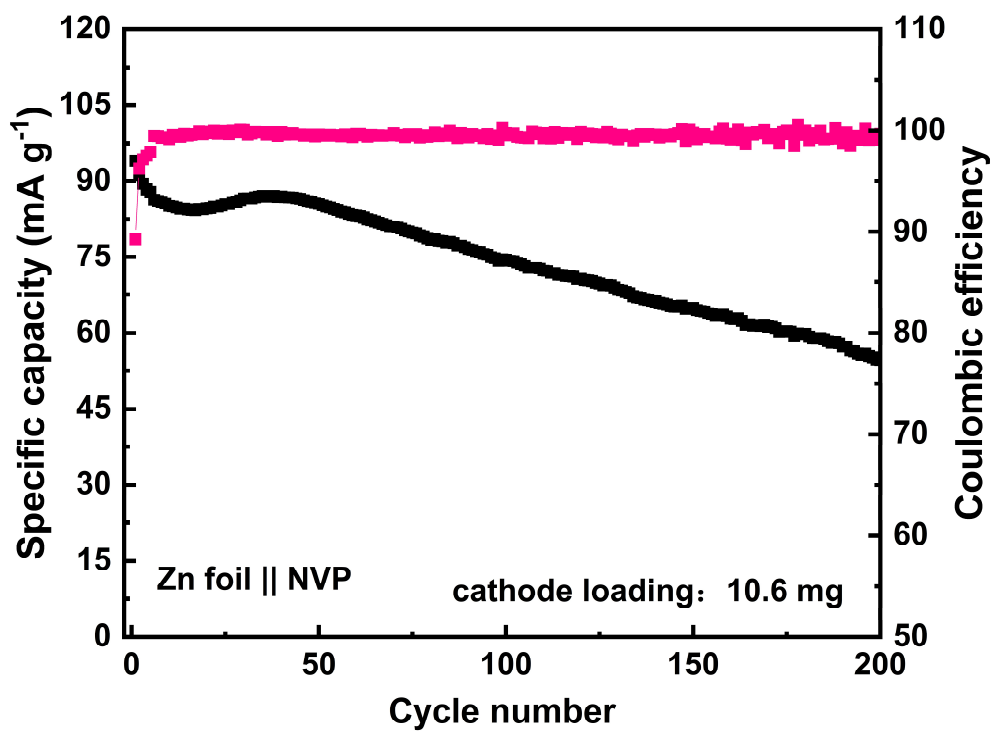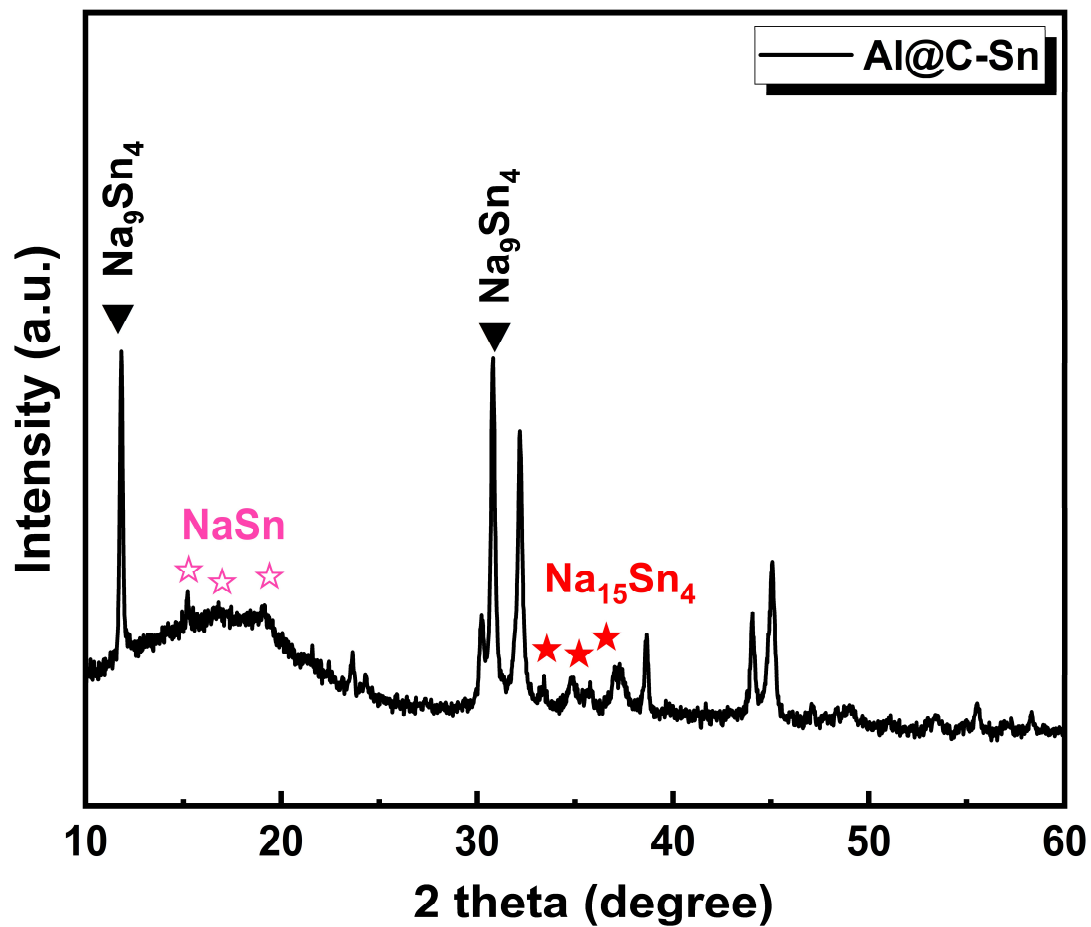
Figure S46. XRD spectra of Al@C-Sn substrate after 5 cycles in a half-cell at 2 mA cm^{-2} in an alloying state (In the alloying stage with sodium, without Na-metal deposition).
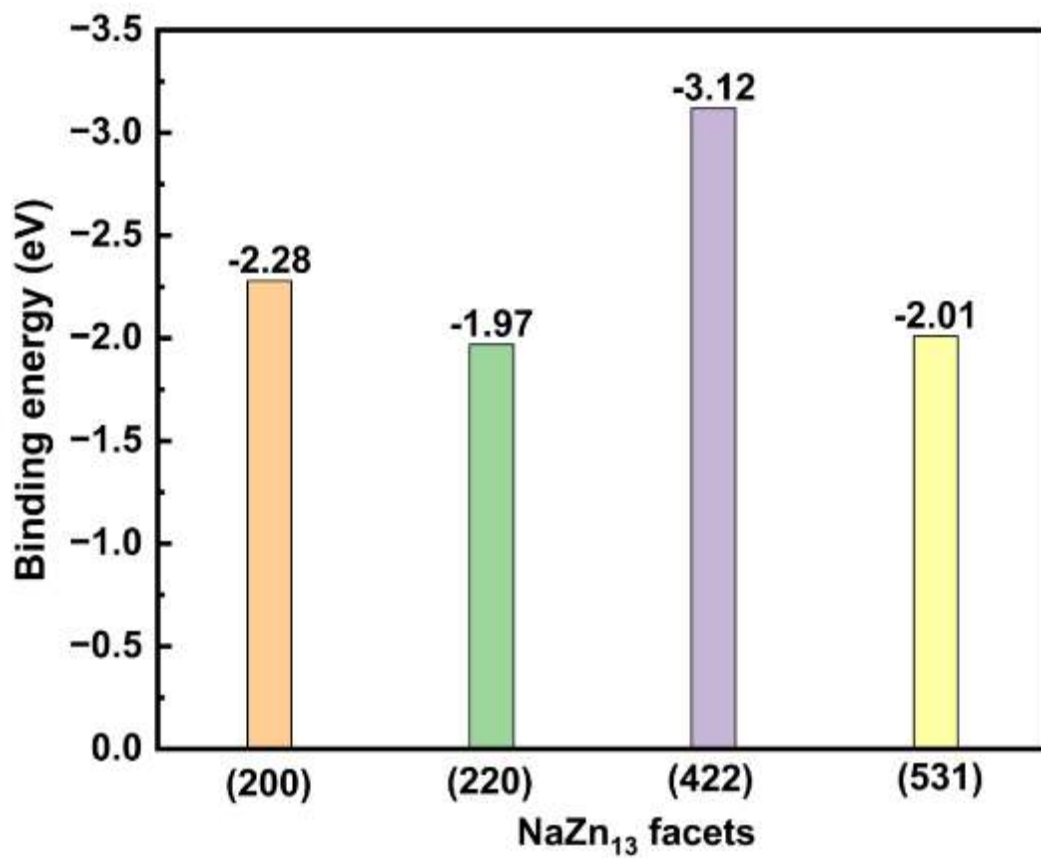
Figure S47. The binding energy of different facets of NaZn$_{13}$ alloy with sodium atoms.

Figure S48. Voltage-time curves for (a) Na‖Al@C, (b) Na‖Al@C-Zn and (c) Na‖Al@C-Sn half-cells at 2 mA cm^{-2} for 2 mAh cm^{-2}. (d) Median discharge voltage curves of Na‖Al@C, Na‖Al@C-Zn and Na‖Al@C-Sn half-cells at 2 mA cm^{-2} for 2 mAh cm^{-2}.

Table S1 Comparison of the cycling performances of the ZSMBs ($Na_3V_2(PO_4)_3$-based) with previously reported works.

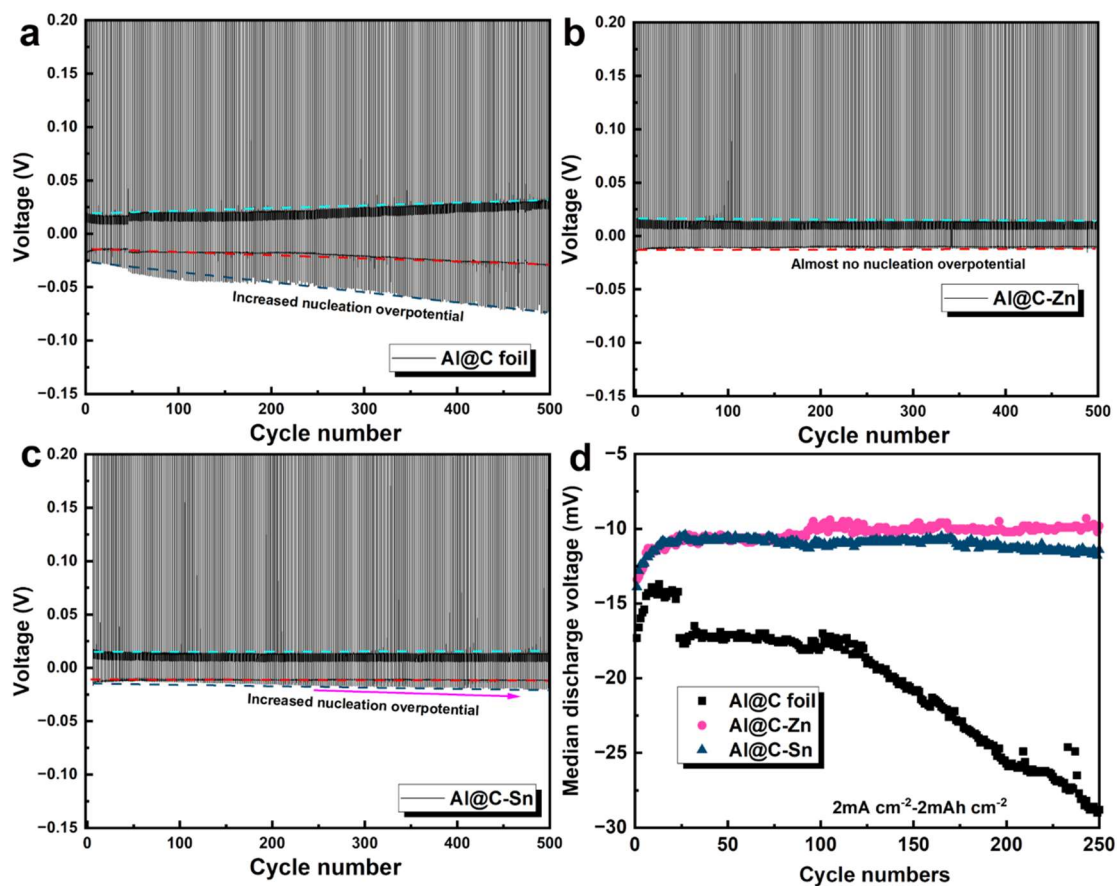| Anode Substrate	cathode	Current density (mA g^{-1})	Cathode loading (mg cm^{-2})	Cycle Number	Average decay rate per cycle	Ref.
Zn@Al	$Na_3V_2(PO_4)_3$	58.5	1.8	100	0.012%	[2]
SnNCNF	$Na_3V_2(PO_4)_3$	234	10	80	0.138%	[3]
Carbon black@Al	$Na_3V_2(PO_4)_3$	38.6	21.4	100	0.175%	[4]
O-CCF	$Na_3V_2(PO_4)_3$	47.2	11	100	0.04%	[5]
PC-CFe	$Na_3V_2(PO_4)_3$	100	10	100	0.03%	[6]
HCOONa-Cu	$Na_3V_2(PO_4)_3$	58.5	~10	400	0.0295%	[7]
Cu	$Na_3V_2(PO_4)_3$	234	2.3	100	0.066%	[8]
Sb/Te alloy	$Na_3V_2(PO_4)_3$	117	2.5	100	~0.23%	[9]
Al-Cu@C	$Na_3V_2(PO_4)_3$	120	3.5–4.0	80	~0.6%	[10]
Al@C-Zn	$Na_3V_2(PO_4)_3$	300	~10.4	200	0.022%	This work
				400	0.034%	
				800	0.041%	

Ref.

1. Y. Zhang, C. Zhang, Y. Guo, and M. Fan, J Am Chem Soc., 2023, **145**, 25643-25652.

2. Cai, Z.; Tang, F.; Yang, Y.; Xu, S.; Xu, C.; Liu, L.; Rui, X., A multifunctional super-sodiophilic coating on aluminum current collector for high-performance anode-free Na-metal batteries. *Nano Energy* **2023,** *116*, 108814.

3. Li, S.; Zhu, H.;　Liu, Y.; Wu, Q.; Cheng, S.; Xie, J., Space-Confined Guest Synthesis to Fabricate Sn-Monodispersed N-Doped Mesoporous Host toward Anode-Free Na Batteries. *Advanced Materials* **2023,** *35* (32), 2301967.

4. Cohn, A. P.; Metke, T.;　Donohue, J.;　Muralidharan, N.;　Share, K.; Pint, Cary L., Rethinking sodium-ion anodes as nucleation layers for anode-free batteries. *Journal of Materials Chemistry A* **2018,** *6* (46), 23875-23884.

5. Li, T.;　Sun, J.; Gao, S.;　Xiao, B.;　Cheng, J.;　Zhou, Y.;　Sun, X.;　Jiang, F.; Yan, Z.; Xiong, S., Superior Sodium Metal Anodes Enabled by Sodiophilic Carbonized Coconut Framework with 3D Tubular Structure. *Advanced Energy Materials* **2021,** *11* (7), 2003699.

6. Lee, K.; Lee, Y. J.; Lee, M. J.; Han, J.; Lim, J.; Ryu, K.; Yoon, H.; Kim, B.-H.; Kim, B. J.; Lee, S. W., A 3D Hierarchical Host with Enhanced Sodiophilicity Enabling Anode-Free Sodium-Metal Batteries. *Advanced Materials* **2022,** *34* (14), 2109767.

7. Wang, C.; Zheng, Y.; Chen, Z.-N.; Zhang, R.; He, W.; Li, K.; Yan, S.; Cui, J.; Fang, X.; Yan, J.; Xu, G.; Peng, D.; Ren, B.; Zheng, N., Robust Anode-Free Sodium Metal Batteries Enabled by Artificial Sodium Formate Interface. *Advanced Energy Materials* **2023,** *13* (22), 2370094.

8. Ma, B.; Lee, Y.; Bai, P., Dynamic Interfacial Stability Confirmed by Microscopic Optical Operando Experiments Enables High-Retention-Rate Anode-Free Na Metal Full Cells. *Advanced Science* **2021,** *8* (12), 2005006.

9. Wang, Y.; Dong, H.; Katyal, N.; Hao, H.; Liu, P.; Celio, H.; Henkelman, G.; Watt, J.; Mitlin, D., A Sodium–Antimony–Telluride Intermetallic Allows Sodium-Metal Cycling at 100% Depth of Discharge and as an Anode-Free Metal Battery. *Advanced*

Materials **2022,** *34* (1), 2270001.

10. Li, H.; Zhang, H.; Wu, F.; Zarrabeitia, M.; Geiger, D.; Kaiser, U.; Varzi, A.; Passerini, S., Sodiophilic Current Collectors Based on MOF-Derived Nanocomposites for Anode-Less Na-Metal Batteries. *Advanced Energy Materials* **2022,** *12* (43), 2202293.